Diesel engines equipped with piezoelectric and solenoid injectors: hydraulic performance of the injectors and comparison of the emissions, noise and fuel consumption

DIESEL ENGINES EQUIPPED WITH PIEZOELECTRIC AND SOLENOID INJECTORS: HYDRAULIC PERFORMANCE OF THE INJECTORS AND COMPARISON OF THE EMISSIONS, NOISE AND FUEL CONSUMPTION

d'Ambrosio, S. , and Ferrari, A*.

Energy Department – Politecnico di Torino

C.so duca degli Abruzzi, 24, 10129, Torino, Italy.

ABSTRACT

A comprehensive comparison between solenoid and indirect acting piezoelectric injectors has been carried out. The working principle of these injector typologies is illustrated, and their hydraulic performance has been analysed and discussed on the basis of experimental data collected at a hydraulic test rig. The injector characteristics, injected flow-rate profiles, nozzle opening and closure delays, injector leakages and injected volume fluctuations have been compared with the dwell time in order to evaluate the impact of the injector driving system.
The solenoid and piezoelectric injectors have been installed on a Euro 5 diesel engine, which has been tested experimentally at a dynamometer cell. Optimized double and triple injection strategies have been considered at some representative key points of the New European Driving Cycle. Engine-out emissions, brake specific fuel consumption and combustion noise are presented and discussed, with the support of a three-zone, diesel combustion diagnostic model. The research has focused on the cause-and-effect relationships between the hydraulic performance of the injectors and the results of the engine tests. The primary goal has been to assess the differences in engine performance between the solenoidal and indirect-acting piezoelectric injector setups are due to the injector driving system or to specific features that are present in the hydraulic circuit of the considered injectors and which are not closely related to the driving system. A final evaluation of the potential of the piezoelectric technology for driving indirect acting injectors is provided on the basis of real engine results.

Keywords: piezoelectric injector; solenoid injector; diesel engine; engine-out emissions; fuel consumption; combustion noise.

Highlights:

-The working principle of indirect acting solenoid and indirect acting piezoelectric injectors is illustrated.
-The hydraulic performance of solenoid and piezoelectric injectors is compared.
-Results of tests on emissions, noise and fuel consumption are discussed for solenoid and piezoelectric injectors.
-Cause and effect relationships between injector hydraulic performance and engine test results are analysed.
- A final evaluation on the effectiveness of the application of piezoelectric injectors to diesel engines is provided.

1. INTRODUCTION

In recent years, the performance of automotive diesel engines has been enhanced significantly and emissions have been reduced greatly as a result of the huge progress that has been made in the development of fuel injection systems. The main goal of improving the diesel fuel injection system is to reduce combustion noise and exhaust emissions, such as *PM* and NO_x, as well as to increase thermal efficiency [1–3].
Even though solenoid-driven injectors for common rail (*CR*) fuel injection systems are widely applied to automotive engines [4], indirect acting piezoelectric injectors represent a valid alternative [5]. Modern, indirect acting piezoelectric

* Corresponding author e-mail address: alessandro.ferrari@polito.it.

and solenoid injectors do not differ only as far as the driving system of the pilot-valve is concerned, they can also often show remarkable differences in the hydraulic layout and mechanical setup.

Therefore, when piezoelectric and solenoid injector samples are compared, it is first necessary to assess the influence of these latter differences on the injection performance in order to be able to evaluate the real benefits that can be derived from the replacement of the pilot-valve actuation system [6].

The solenoid technology is traditionally reliable and cost-effective, and the unit is physically smaller than piezo units. However, solenoid injectors tend to vibrate more than piezo units, thus creating more noise [7]. Furthermore, a piezoelectric injector consumes less power and requires a lower current than a solenoid injector, because a solenoid injector is operated by the peak and hold method, which needs a boosted high operating current for a fast response [8]. Finally, since the fuel pressure tends to close the pilot-valve in piezoelectric injectors, but tends to open this valve in solenoid injectors, the leakage through the pilot-valve is larger for solenoid injectors, and this can represent a limit to the increase in the maximum rail pressure.

Another claimed advantage of piezo-driven injectors is the enhanced dynamic response of the needle [1, 9, 10]: a piezo-stack can generate forces of 800 N [11], while conventional solenoid systems usually show lower values than 100 N [12]. The reduction in the nozzle opening delay (*NOD*) of indirect acting piezo injectors, with respect to solenoid ones, can range from 100 to 150 μs [13], and the time required for the needle to reach the highest position, starting from the rest state, can be reduced by up to 50%, compared to solenoid injectors [11, 10]. Hence, more pressure energy is converted into fuel kinetic energy, and this leads to higher liquid velocities during the needle upstroke. Furthermore, the time required to close the nozzle, that is, the nozzle closure delay (*NCD*), is also less than that of solenoid injectors [11]: the average velocity of the needle during the down-stroke is about 0.7 m/s, whereas it reduces to 0.5 m/s in solenoid injectors [6]. Finally, the multiple injection performance of piezoelectric injectors is generally more flexible, with a minimum interval between fusion free consecutive injections that is less than half that of the minimum interval pertaining to standard solenoid injectors [4].

However, solenoid *CR* injectors have recently witnessed important developments that have partially solved some of their main weak points. It is nowadays possible to realize high-speed solenoids, which feature a faster dynamic response than conventional ones, by optimizing some of the magnetic and electric circuit parameters [14].

These innovative pressure-balanced pilot-valve layouts allow the injector leakage to be significantly reduced [15, 16]: the measured injector static leakages have resulted to be about 25% lower than those of solenoid injectors equipped with standard pilot-valves, even though it still remains higher than that pertaining to piezoelectric injectors. When the pressure-balanced pilot valve layout is coupled to an integrated Minirail injector, the leakage can reduce to 50%, compared to conventional solenoid injectors.

Another merit of the pressure-balanced pilot-valve is that it represents an efficient way of further improving solenoid injector promptness [17]. Finally, the reduced weight of the pressure-balanced pilot-valve leads to a decrease in the required magnetic force of about 35%, compared to standard unbalanced solenoid injectors [17]. Consequently, less electrical energy is required to activate the injector.

As far as modern indirect acting piezo-injectors are concerned, two kinds of hydraulic setups are commonly applied: layouts that feature a 3-way pilot-valve [18] and layouts that feature a bypass-circuit [6]. Both of the devices act on the dynamics of the injector control chamber, which is located at the rear of the needle. The 3-way pilot-valve is aimed at reducing dynamic leakage, that is, leakage through the pilot valve, when this is open, whereas the bypass is aimed at improving the needle dynamic response during the nozzle closure phase.

Piezoelectric injectors generally seem to offer wider margins for optimizing diesel combustion than conventional solenoid injectors [19]. Piezo-driven injection systems have a smaller droplet size, a higher droplet velocity and a larger cone angle (about 10° larger) than solenoid-driven injection systems; all this is probably due to a more rapid opening of the injector nozzle [20]. The more effective vaporization of the fuel spray of piezoelectric injectors could solve the problem related to the presence of film phenomena on the chamber walls and improve the spatial distribution of the fuel and flame in the combustion chamber. On the other hand, the experimental results show that spray tip penetration is not influenced significantly by the injector driving system [20]. In fact, although the liquid jet penetration of piezo injectors is higher than that of solenoid injectors, the wider spray cone angle of piezo injectors makes it dissipate quickly [4].

Despite all the previous studies on hydraulic performance and fuel spray, which hypothesized the superiority of piezoelectric injectors [1-3], the effects of the injector driving system on the emissions, fuel consumption and combustion noise of a commercial automotive engine have not yet been fully revealed [4, 7]. This is an important point for the optimized design of sustainable diesel engines. For this reason, the present work is aimed at comparing the engine performance of piezo-driven and solenoid-driven injectors under various working conditions. The considered solenoid injector features a pressure-balanced pilot valve and is equipped with an integrated Minirail, whereas the piezo-injector

is endowed with a bypass circuit. The analysis at the dynamometer cell was preceded by a comprehensive investigation at the hydraulic rig. The investigation focused on the cause-and-effect relationships between the hydraulic performance of the injectors and the results of the engine tests. This allowed the effective potentiality of the application of the indirect acting piezo technology to diesel engines to be assessed.

2. EXPERIMENTAL FACILITIES AND TESTED COMPONENTS

The analysed CR injection system consists of a rotary pump equipped with a fuel metering valve (*FMV*) [21], a 20 cm^3 rail featuring both a pressure control valve (*PCV*) and a pressure sensor, 200 mm long injector supply pipes with an internal diameter of 3 mm and four indirect acting electroinjectors. Two series of *CR* injectors have been considered: the first is constituted by four indirect acting piezoelectric (*IAP*) injectors and the second by four indirect acting solenoid (*IAS*) injectors. The two typologies of injectors feature the same nozzle and the same maximum pressure level (2000 bar), and both of them have a ballistic needle with the same key features.

A first experimental campaign was aimed at testing the hydraulic performance of the injectors and it was conducted on the Moehwald-Bosch hydraulic test bench installed in the Politecnico di Torino *ICEAL* [12]. The test rig is equipped with several instruments to measure the instantaneous injected flow-rate, the injected volume and injector leakage, the electrical current time distribution to the injector driving system as well as the pressure time histories and temperature levels at different locations along the high-pressure circuit of the injection apparatus. ISO-4113 oil was been used as the working fluid, since it is able to simulate diesel fuel at low temperatures.

An *EVI* flowmeter was applied to evaluate the instantaneous injection rate [22]. The injected flow-rate generates a pressure wave, which propagates in the *EVI* oil-filled pipe. The amplitude of this pressure wave (p_{EVI}) is monitored at the *EVI* pipe inlet, by means of a piezoelectric transducer (its accuracy is 1% of the full scale at 100 bar). The *EMI2* device is used to determine the injected volume by gauging the displacement of a piston, which runs in a chamber in which the fuel is injected, by means of a linear variable differential transformer (*LVDT*). A temperature sensor allows the fluid density to be evaluated, and the injected mass can therefore be calculated. The maximum measurable injected volume is 600 mm^3 and the sensor has an accuracy of 0.1% (≈0.6 mm^3). Finally, KMM continuous flowmeters were applied to detect the volumetric injector leakages [17, 22].

The *IAP* and *IAS* injectors were then installed on a Euro 5 diesel engine, the performance of which had been investigated experimentally. The main features of the tested engine are reported in Table 1: it is a low-compression ratio engine, fueled with conventional diesel fuel and characterized by high EGR rates. The twin-stage turbocharger is used to increase the full load *bmep* to about 25 bar and the engine transient performance, but it is not fully exploited in most of the NEDC area or in the entire PCCI working zone, which occurs at low load and speed conditions for the considered engine.

The experimental tests on the engine were carried out on the AVL dynamic test bed, installed at the Politecnico di Torino ICEAL [23, 24]. The test facility is equipped with a raw exhaust-gas analyzer, which is made up of three analyzer trains. One of these trains has been used, in the present investigation, to measure the NO_x, CO, CO_2, HC and O_2 levels in the engine-out gases. A second train has been employed to detect the CO_2 concentrations in the inlet manifold, in order to calculate the EGR mass fraction, which is defined as $X_{EGR} = \dot{m}_{EGR}/(\dot{m}_{EGR} + \dot{m}_a)$, where $\dot{m}_{EGR}$ is the *EGR* flow-rate and $\dot{m}_{air}$ is the inducted air flow-rate, and is evaluated according to a previously developed procedure [25]. The third train is usually applied to detect the NO_x, CO, CO_2, HC and O_2 levels downstream of the aftertreatment system, but these data have not been measured in the present analysis since no after-treatment device was installed for the performed tests.

As far as the *PM* measurement is concerned, the dynamic test bed is equipped with the following instruments: an AVL 415S smokemeter, an AVL 439 opacimeter and an AVL SPC472 Smart Sampler. Finally, an 'AVL KMA 4000 Methanol' measuring system, with a reading accuracy of 0.1%, continuously meters the engine fuel consumption over the 0.28-110 kg/h range.

A high-frequency piezoelectric transducer was installed on the engine cylinder head to measure the pressure time-history of the gases in cylinder #2, and a high-frequency piezoresistive transducer was used to detect the pressure levels in the inlet runner of the same cylinder in order to reference the in-cylinder pressure. An AVL 365C crank-shaft driven encoder generates the time base for an automatic data-acquisition system, which is managed by AVL Indicom software, in order to allow both the online analysis of the indicated cycle and data storage operation for post-processing with a three-zone combustion diagnostic tool. In this tool [26], the combustion chamber content is divided into three zones: a fuel zone, an unburned gas zone (containing fresh-air, residual gas and *EGR*) and a burned gas zone, obtained from a global stoichiometric combustion process. Ordinary differential mass and energy conservation equations are applied to the three zones and are solved numerically, while the experimental in-cylinder pressure and injected flow-rate time histories are

provided as input data. The model allows the temperatures of the three zones to be calculated as functions of the crank angle. Furthermore, thermal and prompt *NO* mechanisms are implemented in the simulation code, according to the Zeldovich and Fenimore submodels, respectively. Soot formation is modeled [27] by means of the Hiroyasu empirical expression, which considers the mean air-fuel ratio over the combustion interval, whereas the soot oxidation rate is modeled using the Nagle and Strickland-Constable model.

2.1 IAP injectors

A schematic of a piezoelectric injector is reported in Fig. 1 [6]. The nozzle-feeding pipe (Fig. 1a) conveys the oil from the injector inlet to the delivery chamber. The latter is then connected to the upstream chamber of the sac through an annular passage that is delimited by the needle and the injector body. Access of the fuel to the sac (restriction R_4 in Fig. 1d) and to the injection holes (restriction R_5) is regulated by the needle-valve lift.

The main feature of the injector is the presence of a control chamber (Figs. 1a -1c), which is supplied by fuel through a calibrated hole (Z in Figs. 1a-1c). The fuel pressures in the delivery chamber (Fig. 1a), in the upstream chamber of the sac (Fig. 1d) and in the sac (Fig. 1d) induce opening forces on the needle, whereas the pressure in the control chamber gives rise to a closure force on the needle. When the piezo-stack is not activated, the pressure value in the control chamber approaches the rail pressure level. Hence, the hydraulic force acting at the rear of the needle, together with the needle-spring preload, overcome the force due to the pressure acting on the shoulder of the needle in the delivery chamber (Fig. 1a) and on part of the needle tip in the upstream chamber of the sac (Fig. 1d). As a result, the needle is pressed into its seat and seals off the passage of the high-pressure fuel to the combustion chamber via the sac.

As the electric current to the injector is supplied by the electronic control unit (*ECU*), some of the charge is stored in the piezo-stack (cf. the actuator in Fig. 2), which is 7 mm × 7 mm × 32.7 mm and has an electrical capacitance of ~4.6 μF; this induces axial elongation of the piezo-material. The elongation is then converted into a displacement of the pilot-valve by means of a hydraulic amplifier (Fig. 2). The amplification factor of the piezo-stack elongation depends on the ratio (>1) of the cross-section of the upper piston that enters the hydraulic amplifier (piezo-stack actuator) to the cross-section of the lower piston that leaves the hydraulic amplifier (pilot-valve stem). The descent of the pilot valve closes off the bypass (Figs. 1b and 1a) and makes hole A operative for fuel discharge: the control chamber is connected to the tank through a return pipe, and this allows the control chamber to be emptied. The pressure in this chamber decreases, as does the hydraulic force, which acts at the rear of the needle. As soon as the force due to the difference between the delivery-, the sac- and the control-chamber pressures prevails over the needle-spring preload, the needle moves upwards and some fuel is admitted, through the injection holes, into the engine cylinder.

When the piezo stack is discharged at the end of the energizing time, the piezo-stack actuator withdraws and the fuel pressure in the hydraulic-amplifier chamber (Fig. 2) falls. As a consequence, the pilot valve is forced upward by the spring that acts on it, and there is a renewed build-up of pressure in the control chamber, which is caused by the fuel flowing in from holes Z and A (Fig. 1c). In fact, the bypass is now open and some fuel can flow from the delivery chamber to the control chamber through hole A. Therefore, unlike solenoid injectors, the A hole in piezo-injectors can work not only as a fuel discharger, but also as a fuel supplier. This is why such a hole is also referred to as the A/Z throttle in the piezo-injector context (the Z hole always acts as a fuel supplier). Even though the main flow-rate that enters the control chamber during the needle downstroke occurs through the Z hole, the contribution through the series of the bypass and hole A is significant [6]. Numerical analyses have proved that the bypass flow tends to significantly reduce the time required to slowdown the needle during its upstroke and the subsequent time required to cover the needle downstroke.

2.2 IAS injectors

The internal dynamics of the tested indirect acting solenoid injectors (Fig. 3) is qualitatively very similar to that of piezoelectric indirect acting injectors [6, 28]. When the electrical current to the injector solenoid is switched on, the pilot valve is lifted up because of the action of the electromagnetic force on the pilot-valve armature (Fig. 3b); some fuel is therefore discharged from the control chamber to the tank, the needle opens the nozzle through the same mechanism as in the case of the IAP injector and injection occurs. As soon as the current to the solenoid is switched off, the closure of the pilot-valve makes the pressure rise in the control chamber, thus inducing the needle closure phase.

No bypass is present in the hydraulic circuit of solenoid injectors, and this causes a slower refilling of the control chamber at the end of the energizing time, thus reducing the needle velocity during the downstroke. The solenoid injector that is considered in the present work features a pressure balanced pilot-valve layout (Fig. 3b), which reduces the pressure force acting on the pilot-valve, compared to the case of the pressure-unbalanced standard layout (cf. Fig. 3c). In the pressure-

balanced pilot-valve in Fig. 3b, the fuel pressure action mainly results in a vertical force that acts on a fixed rod, which is mechanically linked to the injector body, and in a radially balanced mechanical action (F_r) on the inner surface of the valve armature. Furthermore, the forces acting on surfaces *S'* and *S''*, that is, *F'* and *F''*, counterbalance each other and therefore do not introduce any net force that could lift the armature. Contact between the armature and the injector body occurs along a small annular surface (*S*) bounded by diameters d_1 and d_2. As already mentioned, the development of the pressure-balanced pilot-valve is mainly justified by the necessity of increasing the maximum rail pressure without excessively raising the static leakage and the magnetic force [17]. A reduction in the opening hydraulic force (F_p) can be obtained by diminishing the mean diameter, $d=(d_1+d_2)/2$. However, the stroke-end of the valve must be increased in order to maintain the required design value for the pilot-valve restricted flow-area: this requires a higher magnetic force and leads to a worsening of the dynamic performance of the mobile pilot-valve element. In general, the stroke-end design value of the valve is a compromise between the optimization of the dynamic response of the armature and the minimization of the static leakage: the lower the stroke-end value, the prompter the dynamic response of the mobile elements, but also the larger the static leakages, because of the larger *d* diameter [17].
Another remarkable feature of the considered solenoid injector is the presence of a 2.5 cm^3 Minirail that is integrated in the delivery chamber (Fig. 3a). This accumulation volume, which is not present in the piezoelectric injector in Fig. 1 or in many solenoid injector designs, leads to a more stabilized delivery-chamber pressure level during the injection, to a more rectangular injected flow-rate shape and to an increased needle-lift peak value [29]. Furthermore, the Minirail layout eliminates the low-pressure environment that is located between the delivery and the control chambers in solenoid and indirect acting piezoelectric injector hydraulic layouts (in Fig. 1a, this environment is where the needle spring is located). As a result, since the same pressure levels exist at the extremities of the L_1 and L_2 annular channels (Fig. 3a), two important leakage paths, which that contribute significantly to the static leakage of standard (i.e. without Minirail) indirect-acting solenoid injectors, are removed.

3. HYDRAULIC PERFORMANCE

Figure 4 reports the injector characteristics, that is, the injected mass (*M*) as a function of the energizing time (*ET*) at different nominal rail pressure (p_{rail}) levels, for the two types of tested injectors. Fig. 4a refers to the *IAP* injector, whereas Fig. 4b refers to the *IAS* injector. Each characteristic refers to a statistical group of injectors, and its thickness is related to injector-to-injector dispersion: the higher the thickness, the higher the injector-to-injector dispersion on *M*.
The flow-capability of the considered *IAS* and *IAP* injectors is very similar for fixed values of *ET* and p_{rail}. This occurs since the two considered injector types feature the same nozzle and the same conical angle and geometrical sizes of the needle. The injector characteristics in Figs. 4a and 4b increase almost linearly with the energizing time for 500 μs $\leq ET \leq$1400 μs, because the needle is ballistic in both the *IAS* and *IAP* injectors. A nonlinear trend of *M,* with respect to the energizing time, is observed in the $ET \leq$500 μs range, but the behaviour of the injector characteristics continues to be similar for the two injectors, even in this operation zone. The general dependence of *M* on the nominal rail pressure is regular in both cases, because the injected mass for fixed *ET* always increases with the value of p_{rail}.
Table 2 reports data on the injector-to-injector dispersion for different p_{rail} values of the *IAS* and *IAP* injectors. The mean injected quantity (M_{inj}) and the corresponding injector-to-injector variability (ΔM_{inj}) of the statistical group of tested injectors is reported for different working conditions (ΔM_{inj} is the maximum difference between the injected masses pertaining to all the injectors of the same family at each working condition). As can be inferred, the *IAS* injector features a higher injector-to-injector variability than the *IAP* injector when both *ET* and p_{rail} take on medium to high values, but exhibits better results at low p_{rail} levels (cf. results at 500 bar) and at very low *ET* values (cf. results at the smallest injected masses). These conclusions are coherent with the thickness of the injector characteristics shown in Fig. 4 (the characteristics are thicker for the *IAS* injector at high *ET* and p_{rail} values). However, the maximum injector-to-injector dispersion at p_{rail}=1800 bar and $M\approx$100 mg is around 7.5% for the *IAS* injector and is therefore acceptable (the threshold is 15-20% for Euro 6 automotive injectors without compensation codes).
ET_{min} is the minimum energizing time for which the injected quantity, measured by means of the *EMI* device, shows a lower cycle-to cycle standard deviation than 10% [30]. ET_{min} and the minimum stable injected quantity are reported in Fig. 5 as a function of the nominal rail pressure for the two injector types: each value represents an average of a statistical group of injectors of the same family. The minimum repeatable quantity varies from 0.2 mg to 0.35 mg for both the *IAP* and *IAS* injectors, which therefore show similar performances in controlling small quantities. The correct dosage of tiny amounts of fuel is critical in *CR* fuel injection systems, because the injection pressure is very high, even during the needle-

opening phase, due to the presence of a pump, a pressure control system and a rail, which continuously generate and maintain the high-pressure level.

Figure 6 reports the volumetric injector leakage ($V_{leakage}$), which is the sum of the static and dynamic leakages per engine cycle. Static leakage is the clearance leakage through the injector when the pilot-valve is closed, whereas dynamic leakage is the leakage per engine cycle that occurs through the pilot-valve when the electrical current to the injector is switched on. Dynamic leakage increases with the value of *ET*, whereas static leakage mainly depends on p_{rail}, even though a weak effect of *ET* is also present for the static leakage. In fact, since the average temperature of the fuel within the injector increases with *ET,* and the fuel viscosity, which affects the laminar leakage flow, reduces for an increasing fuel temperature, the static leakage weakly augments with *ET* [17].

The total leakage of the *IAS* injector is similar to that of the *IAP* injector at p_{rail} =1600 bar and *ET*=1000 μs. Furthermore, Fig. 6 shows that the volumetric static leakage, evaluated as the injector leakage per engine cycle for $ET \rightarrow 0$, tends to be higher for the *IAS* injector, especially for the highest p_{rail} values. This is definitely confirmed by the data in Table 3, which show that the *IAS* injector features a higher static leakage than the *IAP* injector, even though the static leakage of the considered *IAS* injector is smaller than the typical ones of solenoid injectors. Since the fuel pressure tends to close the pilot-valve in the *IAP* injector, its static leakage does not increase significantly with the rail pressure level in Table 3.

On the other hand, the slope of the $V_{leakage}$ versus *ET* curves at each p_{rail} shown in Fig. 6 is higher for the *IAP* injector, and this proves that its dynamic leakage is larger. As a result, the total leakage of the *IAS* is lower than that of the *IAP* when the dynamic leakage becomes the most relevant contribution to $V_{leakage}$ (this happens for $p_{rail} \leq$800 bar and for medium to high *ETs* at p_{rail} =1000 bar and at p_{rail} =1200 bar). Instead, the $V_{leakage}$ of the IAS injector is higher when the static leakage is the most important part of $V_{leakage}$ (this occurs at p_{rail} =1600 bar and, for small to medium *ETs*, at p_{rail} =1200 bar).

Figures 7-9 plot the injection rate (measured as p_{EVI}) and injector-inlet pressure ($p_{inj,in}$ is measured along the rail-to-injector pipe) time histories of the IAP and IAS injectors for different working conditions of *ET* and p_{rail}; furthermore, the current time history is also reported. The flow-rate shape is generally almost rectangular for the *IAS* injector for medium and high *ET* values; in particular, the flow-rate values that occur in correspondence to the final portion of *ET* are slightly higher for the *IAS* injector. Furthermore, the triangular flow-rate time histories plotted in Fig. 7, under a low *ET* value, show a higher peak value for the *IAS* injector. All these differences are due to the presence of the integrated Minirail in the *IAS* injector. The needle velocity and the needle-lift peak value always increase in the presence of the Minirail for fixed p_{rail} and *ET* values, because the opening pressure force on the needle is higher during the upstroke [29]. In fact, the delivery chamber pressure decrease that follows fuel injection is smaller when a Minirail is integrated in the injector hydraulic circuit, and this allows the pressure force acting on the needle to be intensified.

The fuel injection finishes later for the *IAS* injector in Figs. 7-9 and, since the start of injection is almost the same for the two injector-types, the effective injection duration and the injected mass result to be larger for the IAS injector.

Figures 10 and 11 report the nozzle opening delay and the nozzle closure delay, respectively, for the *IAP* (*a*) and *IAS* (*b*) injectors. The nozzle opening delay is exactly the same as the time interval between the start of electrical current signal rising and the instant at which fuel injection begins. Instead, the nozzle closure delay is the difference between the time instant of the electric current shut-off (for the piezo injector, this corresponds to the instant at which the current becomes negative) and the instant at which the nozzle definitely closes.

For indirect acting injectors, *NOD* is roughly the sum of the time required to discharge the control chamber and the time necessary to regain the nozzle axial deformation [28]. The *NOD* in Fig. 10 generally reduces with the rail pressure level, consistently with what is documented for indirect acting injectors [28]. The values of *NOD* are similar for the *IAS* and *IAP* injectors, because the nozzle opening delay depends on the volume of the control chamber, on the diameters of the A and Z holes, on the needle spring preload as well as on the geometry and material of the needle: most of these parameters are the same for the two considered injectors.

The *NCD* mainly depends on the maximum needle-lift value. As soon as the needle reaches its stroke-end (whenever it is reached within the working area), the NCD remains constant. It is therefore confirmed, from the results in Fig. 11, that the needle is ballistic for both the IAS and the IAP injectors, since *NCD* continuously grows with *ET*. Furthermore, *NCD* is larger for *IAS,* because *IAP* features the bypass duct, which can significantly reduce the nozzle closure delay [27], and because the Minirail also gives rise to higher needle-lift peak values. Since the injection temporal length (*ITL*) is equal to $ITL=ET+NCD-NOD$, *NCD* is higher for *IAS*, and *NOD* is almost the same for the two injectors, the injection duration is generally higher for the *IAS* injector, as is shown in Fig. 12. In the case of *IAP*, the smaller difference between *ITL* and *ET* can help to achieve an enhanced control of the injection phasing (*ITL* should ideally be equal to ET for an optimum control of injection phasing).

3.1 Multiple injection performance

In the injector inlet pressure ($p_{inj\,,\,in}$) time histories plotted in Figs. 7-9, the pressure fluctuations that are induced by the water hammer at the end of the injection event feature lower frequencies in the case of the *IAS* injector because of the presence of the Minirail. Fig. 13 reports the injected mass variations as a function of dwell time (*DT*) in the pilot-main injections with nominal injected masses of M_{pil}=1 mg and M_{main}=19 mg for two different p_{rail} levels (1000 bar and 1500 bar). The ΔM quantity represents the variation in the total mass ($M= M_{pil}+M_{main}$), which is injected under a certain *DT* value, with respect to the nominal value (20 mg). This variation is due to pressure oscillations, which propagate thorough the high-pressure circuit. Since the pilot injection is the former shot, M_{pil} is not affected by any pressure waves triggered by previous injections; therefore, the changes in *M* virtually coincide with those in $M_{main,}$ and are due to the pilot-injection-induced pressure oscillations, which arise as a result of the nozzle closure because of the water hammer.
The higher frequency of the basic *M* fluctuations, pertaining to the *IAP* injector in Fig. 13, is consistent with what occurs in the $p_{inj\,,\,in}$ pressure oscillations at the end of the injection in Figs. 7-9. However, high-frequency oscillations can be detected for the IAS injector in Fig. 13b, in addition to the basic fluctuations with a time period that also exist in the $p_{inj,in}$ traces (T_{IAP}). Furthermore, the maximum amplitude of the ΔM oscillations, with respect to *DT,* is similar for the two injector types, even though the amplitude of the $p_{inj,in}$ waves are appreciably higher for the *IAP* injector in Figs. 7-9. The main differences in the pressure wave and multiple injection performance between the *IAS* and *IAP* injectors are related to the presence of the Minirail in the *IAS* injector. The scheme in Fig. 14 tries to clarify the effect of the Minirail on the pressure wave dynamics that is triggered by an injection event. When a pressure wave, which is triggered by the injection and arises in the nozzle, reaches the Minirail (this can be regarded as a pure hydraulic capacitance element in this analysis), part of the incoming wave is transmitted downstream from the capacitance to the injector-inlet pipe and part is reflected back toward the nozzle. As the Minirail volume increases, the amplitude of the reflected wave becomes larger, whereas that of the transmitted wave becomes smaller: a significant number of unsteady waves therefore travel back and forth between the nozzle and the injector delivery chamber. The disturbances induced on the nozzle dynamics by the Minirail-reflected pressure waves are probably responsible for the high frequency fluctuations in the *M* versus *DT* diagrams in Fig. 13. On the other hand, the Minirail-transmitted pressure waves have a lower amplitude than that of the pressure waves generated in the nozzle and, as a result, the pressure fluctuations in the $p_{inj\,,\,in}$ traces in Figs. 7-9 feature smaller amplitudes in the presence of the Minirail. In other words, since the Minirail tends to decouple the time history of the pressure in the nozzle from the $p_{inj\,,\,in}$ time history, the dynamic performance of the IAS injector can be misunderstood if conclusions are only made on the basis of $p_{inj\,,\,in}(t)$.
The basic period (T_{IAP} or T_{IAS}) of the pressure waves travelling along the injector-inlet pipe is generally influenced by the geometry of the high-pressure circuit, from the nozzle to the rail, and the basic period increases when the accumulation volume of the circuit increases [29]: this explains why the period of the $p_{inj,in}$ oscillations augments in Figs. 7-9 for the injector integrated Minirail layout. In the case of the IAS injector, the complex interaction, which occurs between the high-frequency pressure waves (the Minirail reflected waves) and the low-frequency pressure waves in the nozzle with the T_{IAS} period, gives rise to oscillations which have almost the same maximum amplitude as those corresponding to the IAP injector, as can be observed in the *M* versus *DT* diagrams in Fig. 13.

4. EXPERIMENTS ON THE ENGINE AT THE DYNAMOMETER CELL

Tests have been carried out at the dynamometer cell to evaluate the differences, in terms of pollutant emissions, combustion noise (*CN*) and brake specific fuel consumption (*bsfc*), for the same engine equipped with either the solenoid or the piezoelectric injectors.
Optimized pilot-main (*pM*), pilot-pilot-main (*ppM*) and pilot-main-after (*pMa*) strategies were considered in the comparison and engine tests were performed at some key points in the low-load and low-speed area as well as in the medium load and speed zone. The key points have been considered as representative working conditions of the engine application to a passenger car over the New European Driving Cycle and have been characterized in terms of *bmep* (bar) and speed *n* (rpm)
The tested engine (cf. Table 1) was originally calibrated by the OEM with a *pM* strategy, which represented the state-of-the-art pilot-main injection schedule for the considered engine technology equipped with the *IAP* injectors. All the triple injection strategies were optimized by adopting the design of the experiment (*DoE*) statistical technique [31, 32]. The rail pressure (p_{rail}), the swirl actuator position, the dwell times between consecutive injections, the main injection timing (SOI_{Main}), the injection quantities in each pilot or after shot and the inducted air per stroke and per cylinder were the most important input variables for the *DoE* procedure. Different values of these parameters were considered in the variation

lists for the optimization of the injection schedules at each engine key point. The variation lists were obtained with the Matlab Model-Based Calibration toolbox, by setting a V-optimal type design of experiments, which minimizes the prediction error variance, and by considering a full factorial series as the preliminary candidate set (the final variation lists were made up of 120–150 tests for each considered key-point).
The execution of the thus obtained variation lists was then randomized, and replications of the central point (defined as the center value of each parameter range) were added every 10–15 points in order to further reduce the prediction error variance and check for any possible drifts of the output variables for fixed input parameters.
Once the variation list tests had been carried out, it was possible to obtain quadratic models of the output variables as functions of the input variables and of their interactions. The specific engine-out NO_x, *CO*, *THC* and soot emissions, the *bsfc* and the *CN* were considered as the output variables of the *DoE* procedure. Different targets can be considered for the output variables in order to select the best set of values for the input variables and to obtain the optimized calibration at each key point. The present Euro 5 engine was applied to a vehicle equipped with a diesel oxidation catalyst and a particulate filter, but no aftertreatment device was designed to reduce the NO_x emissions. The optimization strategy for the triple injection schedules, which were developed on the basis of the *DoE*, was therefore aimed at minimizing NO_x emissions and at reducing the combustion noise, compared to the pilot–main injection calibration. However, rather severe targets were also set for *CO*, *HC* and *bsfc*.
The optimization of the triple injection strategies with the *DoE* technique has been carried out for either the *IAP* or *IAS* injectors; the *pM* calibration provided by the OEM for the *IAP* injectors was selected as the starting point to apply the *DoE* procedure. The OEM chose a few engine working points as being representative of the working conditions of the engine application to a passenger car over the New European Driving Cycle: these key points were characterized in terms of speed n (rpm) × bmep (bar) within the 1.5 bar$\leq$*bmep*$\leq$12 bar and 1000 rpm$\leq$*n*$\leq$2750 rpm area. Optimization of the key-points can provide the potentialities of a combustion strategy without the need of performing an optimal calibration of all the possible working conditions. Owing to the long time required to perform the optimization, through *DoE* statistical techniques, the activities were concentrated on a reduced number of key-points, namely at low speed and load, medium-low speed and load and medium speed and load (other combinations are obviously possible, but were not considered for the current activity).
Tables 4–6 report the parameter values that were considered in the variation lists (second column) and the optimization pertaining to the *ppM* injection schedules at the 1500×2 (*n* × *bmep*) and 2000×5 key points (Tables 4 and 5, respectively) and to the *pMa* strategy at the 2500×8 key point (Table 6), for either *IAP* or *IAS* injectors. The corresponding targets for the output variables are reported in Tables 7-9. A postponed timing of the main injection (a negative SOI_{main} means that the start of the electrical current provided to the injector occurs after *TDC*) was applied at 1500x2 in order to enable a late *PCCI* strategy [31]. In general, the presence of a reduced compression ratio and the application of calibration with high *EGR* rates and retarded SOI_{main} induced a low temperature combustion mode [33] at all the tested points.
EGR trade-offs were performed at the dynamometer cell in the neighborhood of the calibration baseline points (optimizations) for each injection strategy and each key point, in order to have a more complete comparison of the two injector types not only for the baseline point of each calibration, but also for complete curves.

4.1 Low load and speed tests

Figures 15-19 compare the emissions, *CN* and fuel consumption of the two-injector typologies along an *EGR* sweep, for the 1500×2 key point and for a pilot-pilot-main (*ppM*) triple injection strategy. The NO_x are always reported as horizontal abscissa in the graphs, and higher NO_x emissions always correspond to lower *EGR* fractions [25] (X_{EGR} varies between about 45% and 55%). The ordinate axis of the graphs reports the engine-out *HC* emissions in Fig. 15, the engine-out *CO* emissions in Fig. 16, the engine-out soot emissions in Fig. 17, the *CN* in Fig. 18 and the *bsfc* in Fig. 19. The *EGR* condition, which refers to the optimized triple calibration of each injector, is indicated with a contoured symbol in the graphs. As can be inferred from Fig. 17, the typical soot-NO_x trade-off of conventional diesel combustion exists for the *IAP* injector, whereas the engine equipped with the *IAS* injectors features a *PCCI*-like behaviour, that is, when the *EGR* fraction increases, both the NO_x and soot emissions reduce. As a consequence, both the soot and NO_x emissions are higher for the *IAP* injector, and are in line with the target values of NO_x and soot reported in Tables 7a and 7b. The high degree of premixed combustion, which is characteristic of *PCCI* combustion systems, is also responsible for the higher engine-out *CO* and HC emissions of the *IAS* injector (cf. Figs. 15 and 16). Furthermore, the combustion noise is higher for the *IAP*, even though the p_{rail} level during the *EGR* sweep is slightly higher in the *IAS* injector calibration (around 520 bar for the *IAP* and around 585 bar for the IAS). In general, when combustion maintains the same mode, the higher the p_{rail} value, the higher the *CN* level; however, a switch from conventional diesel combustion (*IAP* injectors) to *PCCI*-like combustion

(*IAS* injectors) occurs in the present case, and this is the dominant result. Finally, the *bsfc* data plotted in Fig. 19 for the two typologies of injector are similar.

Figures 20-23 report the same variables as Figs. 15-18, but refer to *EGR* sweeps carried out at 2000×2 under a double injection *pM* strategy. In this condition, combustion is of the *PCCI* type for both engine setups, that is, with the *IAS* and *IAP* injectors, even though Fig. 22 shows that the *PCCI* behaviour is more observable for the IAS injector. In fact, the simultaneous reduction in the soot and NO_x, when the *EGR* fraction increases, is more obvious, that is, the slope of the soot versus NO_x curve is generally higher for the solenoid injector. *PCCI* combustion occurrence is in general more likely for the *pM* strategy than for the *ppM* strategy (cf. Figs. 17 and 22), because a general decrease in the local air-fuel ratio takes place in the latter case. The generation of a suitable fuel vapour stratification close to the nozzle, which is obtained with the *ppM* strategy, should reduce the impact of the premixed combustion portion [31].

In this case, the p_{rail}, is the same for the two injectors (around 550 bar) and this proves that the differences in the combustion process between the *IAS* and *IAP* injectors, and in particular the higher tendency of the *IAS* injector to *PCCI* combustion, are not caused by differences in the rail pressure value.

The main point in fact concerns the presence of the integrated Minirail for the *IAS* injector. The Minirail is able to sustain the injection pressure, especially during the first part of the injection event (the injection event tends to make the pressure reduce in the injector delivery chamber, and the Minirail counteracts this tendency), and this is expected to increase the needle velocity in this phase. As a consequence, fuel atomization should be improved during the nozzle opening phase for the *IAS* injector (in other words, a lower Sauter diameter of the fuel droplets can be obtained); this should cause the *IAS* injector to show a higher tendency toward the *PCCI* combustion mode, and can also explain the reduction in the soot production.

The *IAS* injector in Table 4 implements smaller q_{Pil2} and shorter DT_2 than the *IAP* injector. Since the presence of the injector integrated Minirail improves fuel atomization and induces leaner combustion, a reduction in the values of q_{Pil2} and DT_2 is possible for the *IAS* injector, and this can help to support *PCCI* combustion.

Higher engine out *HC* and *CO* emissions can be observed in Figs. 20 and 21 for the engine setup with the *IAS* injectors, and this in line with the more intense degree of *PCCI* combustion that is reached in this case. Furthermore, the *CN* in Fig. 23 continues to be higher for the case of the *IAP* injectors, as it was for the test at 1500×2 under *ppM*. The *bsfc* has not been reported for the 2000×2 working condition, but it has been verified that *IAP* and *IAS* injectors feature almost the same values, as in the case of Fig. 19.

In-cylinder analyses have been conducted to obtain a better understanding of the results of the engine tests. Fig. 24 reports the *HRR* curves of the *IAS* and *IAP* injectors for the baseline calibrations of the *ppM* strategy at 1500× 2. Autoignition of the fuel occurs after the end of the second pilot shot for the *IAS* injector, and the autoignition delay is longer than in the case of the *IAP* injector; this ensures a higher premixing degree of the combustion mixture, in line with *PCCI* behaviour. The leaner combustion makes $dHRR/d\theta$ reduce during the initial phase of the main combustion. The maximum *HRR*, which is related to the value of $(dp/d\theta)_{max}$, pertains to the IAP injector, and *CN* tends to increase with the value of $(dp/d\theta)_{max}$ [34, 35]. Furthermore, the transition between the pilot and main combustion events is smoother for the *IAS* injector: all this can explain the higher *CN* level of the optimized point of the engine equipped with the *IAP* injectors in Fig. 18.

Figure 25 shows that the soot production phase (350 CA<θ<370 CA) is much more intense for the *IAP* injector during the pilot and main combustion, in line with the final soot emission data in Fig. 17. The reasons for this can be found in the lower atomization, due to the lower needle velocity, but also in the higher temperature levels within the combustion chamber, which are due to the more vigorous pilot combustion of the engine with the *IAP* injectors. However, it is worth pointing out that the final soot levels (at θ≈410 CA) in Fig. 25 are not critical for diesel engine passenger cars if a diesel particulate filter is used.

Figures 26 and 27 plot, with thin lines, the *HRR* curves (left y-axis) along the *EGR* sweeps for the *pM* strategy at 1500x2, for the *IAP* and the *IAS* injectors, respectively. The schematized injection rates are also reported in thick black lines (right y-axis). These diagrams are interesting because the same calibration has been applied to the two-injector typologies, while the *HRR* comparison on the triple injection (cf. Fig. 24) was performed by considering the *DoE* optimized calibrations, which are different for the *IAS* and *IAP* injectors.

As can be inferred, the increase in *EGR* up to 50% makes the *HRR* peak decrease more for the *IAS* injector than for the *IAP* injector, and this more obvious effect of the *EGR* in Fig. 27 is consistent with the presence of a PCCI combustion mode. The difference in the *EGR* effect explains the larger differences in *CN* that can be observed in Fig. 23 between the two injectors when the NO_x emissions reduce.

4.2 Medium load and speed tests

Figures 28-30 report the soot, *bsfc* and *CN* as functions of the NO_x for an *EGR* sweep performed at 2000×5 in the presence of a *ppM* injection strategy. Furthermore, Figs. 31-33, 34 and 35 report analogous graphs for the *pMa* and the *pM* strategy at 2000×5, respectively (the *CN* was not available for the tests with the *pM* strategy at 2000×5). Finally, Figs. 36-38 plot the soot, *bsfc* and *CN* as functions of the NO_x for an *EGR* sweep at 2500×8 under a *pMa* injection schedule. The *HC* and *CO* emissions have not been considered since they are not a concern at medium load and speed conditions.

The combustion mode is the conventional one for the diesel engine equipped with both the *IAP* and the *IAS* injectors because a clear soot-NO_x trade-off with respect to *EGR* can be observed for the considered working conditions (cf. Figs. 28, 31, 34 and 36). In general, *PCCI* combustion occurs at low load and speed conditions and, as the load increases, the combustion system switches from *PCCI* to conventional diesel combustion. On the other hand, the high *EGR* rates that are applied, the low compression ratio of the engine and the postponed SOI_{Main} of the injection strategy enable a low temperature combustion mode with reduced engine-out NO_x emissions, even at medium load and speed conditions.

The *IAP* injectors in the medium load and speed zone generally feature a worsened soot-NO_x trade-off and an increased *bsfc*, compared to the *IAS* injectors (cf. the target values in Tables 8a and 8b for 2000x5 and in Tables 9a and 9b for 2500x8). The *IAP* injectors lead to an augment in the engine-out soot emissions, which is particularly obvious in Figs. 28, 31 and 36, that is, in the presence of triple injections. The NO_x engine-out emissions are also higher for the baseline calibration point of the *IAP* injector in Figs. 31 and 34.

The mean penalty introduced by the *IAP* injectors on *bsfc* is around 4% in Figs. 29 (the case of the *ppM* injection strategy at 2000×5), 32 (the case of the *pMa* injection strategy at 2000×5) and 37 (the case of the *pMa* injection strategy at 2500×8), whereas it is lower than 2% in Fig. 35 (the case of the *pM* injection strategy at 2000×5). The differences in leakage between the *IAP* and *IAS* injectors only play a negligible role on *bsfc,* since a 100% reduction in injector leakage generally leads to a *bsfc* improvement of around 1%. The *IAP* injector leakage in Fig. 6 is almost comparable with that of the *IAS* injector for the p_{nom} and *ET* values that refer to the selected key-points in the *NEDC* zone.

The *CN* is about 1.5-2 dB higher for the *IAP* injector in Fig. 30 (*ppM* injection strategy at 2000×5), about 1.5 dB higher in Fig. 33 (*pMa* injection strategy at 2000×5) and about 1-1.5 dB higher in Fig. 38 (*pMa* injection strategy at 2500×8).

In-cylinder analyses are only presented for 2000×5 and for the *pMa* strategy, but the comments and conclusions have been verified to be similar for the other working conditions. Fig. 39 reports the *HRR* and schematic injected flow-rate curves together with the burned fuel mass fraction (x_b) for the *IAP* and the *IAS* injectors. The peak *HRR* value is smaller for the *IAS* injector, probably due to the leaner mixture during the main combustion, and as a result, the combustion noise in Fig. 33 is lower for the engine equipped with this kind of injector. Furthermore, the faster combustion development pertaining to the *IAS* injector in the 370°CA$<\theta<$395°CA interval (cf. the x_b curves) has also been ascribed to the earlier phasing of the after injection, and is responsible for the improved *bsfc*. Finally, Fig. 40 shows that a critical difference emerges in the soot emissions during the main combustion because of a possible difference in the Sauter diameter of the fuel droplets during the main injection. The better atomization of the fuel and the leaner mixture at the beginning of the main combustion are both probably due to the higher needle velocity (i.e. higher injected flow-rate) of the *IAS* injector during the initial part of the injection. Again, this is not a benefit of the solenoidal injector driving technology, but can be ascribed to the presence of the integrated Minirail in the *IAS* injector layout.

It is possible to state, on the basis of the engine results at low and medium engine speeds and loads (multiple injection schedules with conventional *DT* values have been considered), that the indirect acting piezoelectric injectors do not show any advantages with respect to the solenoid injectors. The soot performance of the IAP injectors is generally worse than that of the IAS injectors, a result that is different from what is stated in [3]. In general, the comparison between indirect acting solenoid and piezoelectric injectors is affected significantly by the differences in the hydraulic and mechanical setups of the considered injectors, whereas the role played by the injector driving technology (piezoelectric or solenoidal) is not pivotal.

The main potentiality of the piezoelectric technology concerns the development of the direct acting concept, in which the injector needle is directly actuated by the piezoelectric driving system, without the application of any pilot valve [36-38]. As far as indirect acting injectors are concerned, solenoid injectors with optimized hydraulic and mechanical setups would be the preferred option, due to their reduced manufacturing costs.

5. CONCLUSION

A comparison has been performed between indirect acting piezoelectric and solenoid injectors, on the basis of the results measured at both the hydraulic test rig and the dynamometer cell.

The flow-rate shape is generally more rectangular for the *IAS* injector at medium and high *ET* values. Furthermore, the triangular flow-rate time histories at low *ET* values show a higher peak value for the *IAS* injector. These differences are due to the presence of the integrated Minirail in the IAS injector. The needle velocity, during the needle upstroke, and the needle-lift peak value in fact increase in the presence of the Minirail for fixed p_{rail} and *ET,* because the delivery chamber pressure decrease that results from fuel injection is smaller.

Injector static leakage is higher for the *IAS* injector, whereas dynamic leakage is higher for the *IAP* injector: this leads to a certain amount of compensation. Although the *IAS* injector features a pressure-balanced pilot-valve layout, and the presence of the Minirail eliminates the leakage path between the control piston and its sleeve, the static leakage at the maximum pressure is still much higher than that of the *IAP* injector, because the fuel pressure tends to open the pilot-valve in solenoid injectors. In general, a higher static leakage reduces the maximum p_{rail} that can be reached by the injection system.

In addition to the basic fluctuations with time period T_{IAS} that are noticeable in the pressure time histories measured at the injector inlet, the injected mass versus *DT* sweeps of the *IAS* injector also feature high-frequency oscillations. These high-frequency disturbances are caused by the pressure waves that travel back and forth between the nozzle and the injector integrated Minirail. The dynamic performance of the *IAS* injector can be misunderstood if conclusions are only made on the basis of the $p_{inj\,,in}(t)$ traces: the *IAS* in fact gives rise to *M* versus *DT* oscillations, with almost the same maximum amplitude as those of the *IAP* injector, even though the $p_{inj\,,\,in}$ time oscillations exhibit significantly lower amplitude for the *IAS* injector.

As far as the engine tests at low loads and speeds with the *DoE*-optimized *ppM* strategies are concerned, the typical soot-NO_x trade-off of the conventional diesel combustion can be observed for the *IAP* injector, whereas the engine equipped with the *IAS* injectors features *PCCI*-like behaviour, that is, when the *EGR* fraction increases, both engine out NO_x and soot emissions reduce. As a consequence, both the soot and NO_x emissions are higher for the *IAP* injector. *PCCI* combustion is also responsible for the higher engine-out *CO* and *HC* emissions of the *IAS* injector. This was also reflected by the different target values obtained from the *Do-E* analysis: in fact, it was more difficult for the *IAP* injector to improve soot and NO_x, whereas some criticism problems exist in the optimization of *CO* and *HC* for the *IAS* injector.

In the case of the *pM* injection strategy at low loads and speeds, in which the same double injection calibration has been applied to the two-injector typologies, the combustion is of the *PCCI* type for both of the engine setups, that is, with the *IAS* and *IAP* injectors, even though *PCCI* behaviour is more obvious for the *IAS* injectors.

The needle velocity increase, which occurs during the first part of the injection event as a consequence of the Minirail installation, improves fuel atomization of the *IAS* injector: this leads to *PCCI* behaviour at low loads and speeds and hence the soot production reduces. Furthermore, the combustion noise is higher for the case of the *IAP* injectors for both tests under the *pM* and *ppM* injection strategies. The leaner combustion makes the maximum *HRR* decrease for the *IAS* injector, and *CN* tends to intensify with the peak value of the heat release.

At medium loads and speeds, a conventional diesel combustion mode occurs for the engine equipped with either the *IAP* or *IAS* injectors because a clear soot-NO_x trade-off can be observed. The *IAP* injectors generally feature worse soot emissions and increased *bsfc* (up to 5%) than the *IAS* injectors at the baseline calibration points. The higher premixed portion of combustion in the case of the *IAS* injector is still caused by the Minirail, which determines the higher needle velocity in the first part of the injection and therefore leads to a better fuel atomization. All this is generally responsible for the improvement in the soot emissions and in *bsfc,* because the premixed combustion development is also faster (the quicker the combustion, the lower *bsfc*). The higher static leakage of the *IAS* injector plays a negligible role on *bsfc* in the NEDC zone, and can only worsen the fuel consumption when p_{rail} reaches the highest values. Finally, the *CN* has been confirmed to generally be higher for the *IAP* injector.

In conclusion, the main differences in the hydraulic and engine performance between solenoid and indirect acting piezoelectric injectors can mainly be ascribed to the presence of different layout solutions in the internal circuit of the injectors (such as the bypass, the pressure-balanced pilot-valve and the Minirail) rather than to the injector driving system. If solenoid and indirect acting piezoelectric injectors shared the same internal hydraulic layout, the differences in their performance would be minimal. Therefore, since the manufacturing cost of solenoid injectors is still lower than that of piezoelectric injectors, solenoid technology should be the preferred option when indirect acting injectors are considered.

6. NOMENCLATURE

bmep	brake mean effective pressure
bsfc	brake specific fuel consumption
CA	crank angle degree

CN	combustion noise
CR	common rail injection system
DT	dwell time between consecutive injections
EGR	exhaust gas recirculation
ET	energizing time
HC	unburned hydrocarbons
HRR	heat release rate
IAP	indirect acting piezoelectric injector
IAS	indirect acting solenoid injector
m_a	inducted air per engine cycle and per cylinder
$\dot{m}_a$	fresh air mass flow-rate
$\dot{m}_{EGR}$	exhaust gas mass flow-rate
M	injected mass
$MFB50$	angle at which 50% of the combustion mixture has burned
n	engine speed
NO_x	nitrogen oxides
OEM	original equipment manufacturer
p_{cyl}	in-cylinder pressure
p_{EVI}	injection rate measured as a pressure by the EVI device
p_{rail}	nominal rail pressure level
$PCCI$	premixed charge compression ignition
PM	particulate matter
pM	pilot-main (injection)
pMa	pilot-main-after (injection)
ppM	pilot-pilot-main (injection)
q_{Aft}	volume of fuel injected in the after injection
q_{Pil1}	volume of fuel injected in the pilot 1 injection
q_{Pil2}	volume of fuel injected in the pilot 2 injection
SOI_{Main}	electrical start of the main injection
Sw	swirl actuator position
t	time
T	period of the hydraulic fluctuations
TDC	top dead center
X_{EGR}	mass fraction of exhaust gas recirculation
x_b	mass fraction burned
ΔM	injected mass variability
ϕ	equivalence ratio
λ	relative air-to-fuel ratio
θ	crankshaft angle in the simulations

7. REFERENCES

[1] R. Payri, F.J. Salvador, J. Gimeno, J. De la Morena, 2011, "Influence of injector technology on injection and combustion development – Part 1: Hydraulic characterization", *Applied Energy*, vol. 88, pp. 1068–1074.

[2] Yu Wenbin, Yang Wenming, Balaji Mohan, Tay Kun Lin, Zhao Feiyang, 2017, "Macroscopic spray characteristics of wide distillation fuel (WDF)", *Applied Energy*, vol. 185, pp. 1372–1382.

[3] R. Payri, F.J. Salvador, J. Gimeno, J. De la Morena, 2011, "Influence of injector technology on injection and combustion development – Part 2: Combustion analysis", *Applied Energy*, vol. 88, pp. 1130–1139.

[4] Jo, S.J., Chung, m. C., Kim, S. M., Sung, G. S., and Lee, J. W., 2015, "Experimental investigation and hydraulic simulation of dynamic effects on diesel injection characteristics in indirect acting piezo-driven injector with bypass circuit system", *International Journal of Automotive Technology*, 16, no. 2, pp. 173-182.

[5] Kim, Y. R., and Cho, S. H., 2009, "New technologies for the super clean passenger car diesel engines", *Auto J.*, 31, 5, pp. 14−24.

[6] Ferrari. A., Mittica, A., and Spessa, E., 2013, "Benefits of hydraulic layout over driving system in piezo-injectors and proposal of a new-concept CR injector with an integrated Minirail", *Applied Energy*, 103, pp. 243-255.

[7] Chung, M., Kim, J., Kim, S., Sung, G., and Lee, J., 2015, "Effects of hydraulic flow and spray characteristics on diesel combustion in CR direct-injection engine with indirect acting Piezo injector", *Journal of Mechanical Science and Technology* 29 (6), pp. 2517-2528.

[8] Dober, G., Guerrassi, N., and Karimi, K., 2012, "Mixture preparation and combustion analysis, a key activity for future trends in diesel fuel injection equipment", SIA Diesel Powertrain International Conference "Innovative Technologies for Future Emissions Targets", Rouen, France.

[9] Taylor, C., and Washington, G., 2003, "The application of piezoceramic actuation to direct fuel injection", SAE paper no. 2003-32-0001.

[10] Fettes, C., and Leipertz, A., 2001, "Potential of a piezo-driven passenger car common-rail system to meet future emission legislations – an evaluation by means of in-cylinder analysis of injection and combustion", SAE paper no. 2001-01-3499.

[11] Lee, K., Oh, B., and Sunwoo, M., 2006, "Development of a programmable driver for solenoid- Type 2-way-valve CR injectors, IPC13 Korea, Kyeongju.

[12] Catania, A.E., Ferrari, A., and Manno, M., 2008, "Development and application of a complete common-rail injection system mathematical model for hydrodynamic analysis and diagnostics", *ASME Trans, J Eng Gas Turbines Power*,130(6):062809.

[13] Oki, M., Matsumoto, S., Toyoshima, Y., Ishisaka, K. and Tsuzuki, N., 2006, "180 MPa Piezo CR system" SAE paper no. 2006-01-0274.

[14] Oki, M., Matsumoto, T., Tomishima, Y., and Nagata, K., 2008, "The advanced diesel CR system for achieving a good balance between ecology and economy", SAE paper no. 2008-28-0017.

[15] Jorach, R.W., Bercher, P., Meissonnier, G., and Milanovic, N., 2011, "Common rail system from Delphi with solenoid valves and single plunger pump", MTZ 03/2011,vol. 72.

[16] Matsumoto, S., Date, K., Taguchi, T., and Herrmann, O.E., 2013, "The new Denso common rail diesel solenoid injector", MTZ 021/2013, vol. 74.

[17] Ferrari, A., Paolicelli, P., and Pizzo, P., 2015, "The new-generation of solenoid injectors equipped with pressure-balanced pilot valves for energy saving and dynamic response improvement", *Applied Energy*, vol. 151, pp. 367-376.

[18] Ueda, D., Tanada, H., Utsunomiya, A., Kawamura, J. and Weber, J., 2016, "4th Generation Diesel Piezo Injector Realizing Enhanced High Response Injector", SAE paper, 2016-01-0846.

[19] Koyanagi, K., Oing, H., Renner, G., and Maly, R., 1999, "Optimizing common rail injection by optical diagnostics in a transparent production type diesel engine", SAE paper 1999-01-3646.

[20] Suh, H. K., Park, S. W., Lee, C. S., 2007, "Effect of piezo-driven injection system on the macroscopic and microscopic atomization characteristics of diesel fuel spray", *Fuel*, 86, pp. 2833-2845.

[21] Catania A. E. and Ferrari A., 2011, "Experimental Analysis, Modeling, and Control of Volumetric Radial-Piston Pumps", *ASME Trans., Journal of Fluids Engineering*, 133, Issue 8, pp. Art. No. 081103, pp1-13 - ISSN 0098-2202. DOI: 10.1115/1.4004443.

[22] Catania A.E., Ferrari A., Manno M. and Spessa E., 2008, "Experimental Investigation of Dynamics Effects on Multiple-Injection Common Rail System Performance", *ASME Trans*, *J Eng Gas Turbines Power*, vol. 130(3), Art. No. 032806, pp. 1-13. - ISSN 0742-4795. DOI: 10.1115/1.2835353.

[23] d'Ambrosio S. and Ferrari A., 2012, "Diesel Injector Coking: Optical-Chemical Analysis of Deposits and Influence on Injected Flow-rate, Fuel Spray and Engine Performance", *ASME Trans*, *J Eng Gas Turbines Power*, vol. 134 n. 6, Art. No. 062801, pp. 1-14 - ISSN 0742-4795. DOI: 10.1115/1.4005991.

[24] d'Ambrosio S., Ferrari, A., Spessa, E., Magro, L., and Vassallo, A., 2013, "Impact on Performance, Emissions and Thermal Behavior of a New Integrated Exhaust Manifold Cylinder Head Euro 6 Diesel Engine", *SAE Int. Journal of Engines*, vol. 6 n. 3, pp. 1814-1833 – ISSN 19463936. DOI: 10.4271/2013-24-0128.

[25] d'Ambrosio, S., Ferrari, A., 2015, "Effects of exhaust gas recirculation in diesel engines featuring late PCCI type combustion strategies", *Energy Conversion and Management*, vol. 105, pp. 1269-1280. - ISSN 0196-8904

[26] d'Ambrosio, S., Ferrari, A., 2016, "Effects of pilot injection parameters on low temperature combustion diesel engines equipped with solenoid injectors featuring conventional and rate-shaped main injection", *Energy Conversion and Management*, Volume 110, 15 February 2016, Pages 457-468.

[27] Baratta M., Catania A.E., Ferrari A., Finesso R. and Spessa E., 2011, "Premixed-Diffusive Multizone Model for Combustion Diagnostics in Conventional and PCCI Diesel Engines", *ASME Trans*, *J Eng Gas Turbines Power*, vol. 133 n. 10, Art. No. 102801, pp. 1-13 - ISSN 0742-4795. DOI: 10.1115/1.4003048.

[28] Catania A.E., Ferrari A. and Spessa E., 2009, "Numerical-Experimental Study and Solutions to Reduce the Dwell Time Threshold for Fusion-Free Consecutive Injections in a Multijet Solenoid-Type C.R. System", *ASME Trans*, *J Eng Gas Turbines Power*, vol. 131, Art. No. 022804, pp. 1-14 - ISSN 0742-4795. DOI: 10.1115/1.2938394.

[29] Ferrari, A., Paolicelli, F., Pizzo, P., 2016, "Hydraulic Performance Comparison Between the Newly Designed Common Feeding and Standard Common Rail Injection Systems for Diesel Engines", *ASME Trans*, *J Eng Gas Turbines Power*, Vol. 138(9): 092801-092801-13.

[30] Catania A. E. and Ferrari A., 2012, "Development and Performance Assessment of the New-Generation *CF* Fuel Injection System for Diesel Passenger Cars", *Applied Energy*, 91, Issue 1, pp. 483-495 - ISSN 0306-2619. DOI: 10.1016/j.apenergy.2011.08.047.

[31] d'Ambrosio, S., Ferrari, A., 2015, "Potential of double pilot injection strategies optimized with the design of experiments procedure to improve diesel engine emissions and performance", *Applied Energy*, vol. 155, pp. 918-932. - ISSN 0306-2619

[32] d'Ambrosio, S., Ferrari, A., 2015, "Potential of multiple injection strategies implementing the after shot and optimized with the design of experiments procedure to improve diesel engine emissions and performance", *Applied Energy*, vol. 155, pp. 933-946. - ISSN 0306-2619.

[33] Richard Folkson, 2014, "Alternative Fuels and Advanced Vehicle Technologies for Improved Environmental Performance - Towards Zero Carbon Transportation", Woodhead Publishing, ISBN 9780857095220.

[34] Heywood, J., 1985, "Internal Combustion Engine Fundamentals", McGraw-Hill

[35] Torregrosa, A.J., Broatch, A., Novella, R., Gomez-Soriano, J., Mónico, L.F., 2017, "Impact of gasoline and Diesel blends on combustion noise and pollutant emissions in Premixed Charge Compression Ignition engines", *Energy*, 137, pp. 58-68.

[36] Ferrari A and Mittica A, 2012, "FEM modeling of the piezoelectric driving system in the design of direct-acting diesel injectors", *Applied Energy*, vol. 99, pp. 471-483.

[37] Raul Payri, Jaime Gimeno, Michele Bardi, Alejandro H. Plazas, 2013, "Study liquid length penetration results obtained with a direct acting piezo electric injector", *Applied Energy*, vol. 106, pp. 152–162.

[38] Vicente Macian, Raul Payri, Santiago Ruiz, Michele Bardi, Alejandro H. Plazas, 2014, "Experimental study of the relationship between injection rate shape and Diesel ignition using a novel piezo-actuated direct-acting injector", *Applied Energy*, vol. 118, pp. 100–113.

8 TABLES AND FIGURES

Engine type	2.0L Euro 5
Displacement	1956 cm^3
Bore × stroke	83.0 mm × 90.4 mm
Compression ratio	16.3
Valves per cylinder	4
Turbocharger	Twin-stage with valve actuators and wastegates
Fuel injection system	Common Rail 2000 bar with 7-hole injectors
Specific power and torque	71 kW/l – 205 Nm/l
EGR system type	Short-route cooled EGR

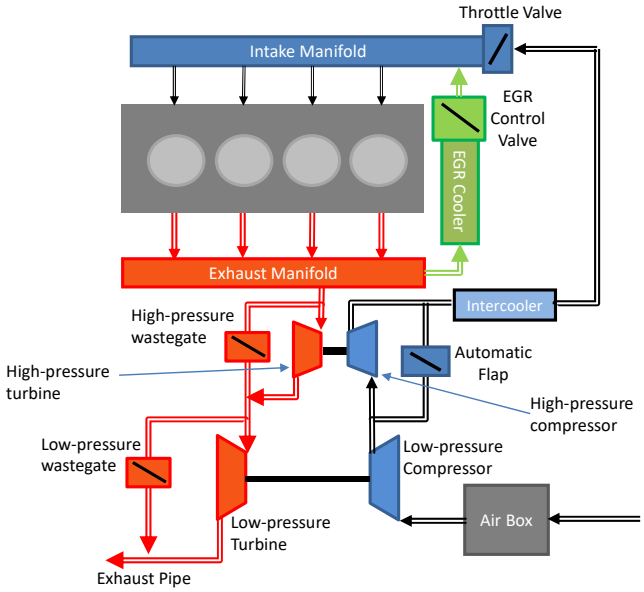

Table 1. Main specifications and schematic of the tested engine.

500 bar		1200 bar		1800 bar	
M_{inj}	ΔM_{inj}	M_{inj}	ΔM_{inj}	M_{inj}	ΔM_{inj}
1.2	0.28	1.9	0.50	1.8	0.85
4.8	0.53	6.6	0.93	10	2.33
12	0.70	20	1.40	40	2.15
25	0.85	40	1.40	56	1.93
40	0.93	51	1.45	80	2.93

(a) IAP injector

500 bar		1200 bar		1800 bar	
M_{inj}	ΔM_{inj}	M_{inj}	ΔM_{inj}	M_{inj}	ΔM_{inj}
1.2	0.10	1.7	0.40	1.6	0.8
5.9	0.20	7.8	1.30	10	3
11.5	0.27	20	1.40	40	3.8
25	0.40	40	1.75	56	4.7
40	0.85	51	2.15	80	5

(b) IAS injector

Table 2. Injector-to-injector dispersion in the injected quantity for different p_{nom} and ET values.

p_{nom} [bar]	IAS [mm³/cyc]	IAP [mm³/cyc]
400	1	1.7
600	2	1.8
800	3.2	2
1000	5	2
1200	7.2	2.1
1400	9.5	2.
1600	12	1.9

Table 3. Static leakage of the indirect acting solenoid and piezoelectric injectors.

Quantity	Levels	Optimization IAP	Optimization IAS
SOI_{Main} [°CA bTDC]	–4.5 –2.88 –1.25 0.37 2	–0.2	0.5
m_a [mm³/(stk·cyl)]	230 245 260	230	237
Sw [%]	30 38.8 47.5 56.3 65	39.7	32.7
p_{Rail}[bar]	300 450 600	516.6	585.0
q_{Pil1} [mm³/(stk·cyl)]	0.8 1.23 1.65 2.08 2.5	1	2.3
DT_1 [µs]	300 625 950 1275 1600	446	485
q_{Pil2} [mm³/(stk·cyl)]	0.8 1.1 1.4 1.7 2	2	0.8
DT_2 [µs]	300 625 950 1275 1600	907	592

Table 4. Variation list and optimization at engine point 1500×2 for the *ppM* strategy.

Quantity	Levels	Optimization IAP	Optimization IAS
SOI_{Main} [°CA bTDC]	–1 1 3	1	1
m_a [mm³/(stk·cyl)]	360 380 390 400 420	362.2	383.2
Sw [%]	30 38.8 47.5 56.3 65	35.5	40.7
p_{Rail} [bar]	750 833.3 950 1016.7 1150	826.4	905.6
q_{Pil1} [mm³/(stk·cyl)]	0.8 1.23 1.65 2.08 2.5	0.8	1.65
DT_1 [µs]	300 625 950 1275 1600	773	970
q_{Pil2} [mm³/(stk·cyl)]	0.8 1.1 1.4 1.7 2	0.8	1.5
DT_2 [µs]	600 850 1100 1350 1600	1600	714

Table 5. Variation list and optimization at engine point 2000×5 for the *ppM* strategy.

Quantity	Levels	Optimization IAP	Optimization IAS
SOI_{Main} [°CA bTDC]	1 3.5 6	5.2	4.2
m_a [mm³/(stk·cyl)]	560 593.3 610 626.7 660	560	560
Sw [%]	10 27.5 45	23.7	24.0
p_{Rail}[bar]	1000 1100 1200 1300 1400	1129	1013
q_{Pil} [mm³/(stk·cyl)]	0.7 1.1 1.5	0.7	0.7
DT_{Pil} [µs]	600 850 1100 1350 1600	1600	1018
q_{Aft} [mm³/(stk·cyl)]	0.7 1.25 1.8 2.35 2.9 3.45 4	0.72	1.42
DT_{Aft} [µs]	800 1000 1200 1400 1600	885	800

Table 6. Variation list and optimization at engine point 2500×8 for the *pMa* strategy.

Strategy	NO_x [g/kWh]	HC [g/kWh]	CO [g/kWh]	Soot [g/kWh]	bsfc [g/kWh]	CN [dBA]
pM	0.53	2	8.8	0.04	299	79.7
ppM	min	≤2	≤9	≤0.3	≤305	≤78

(a) IAP injector

Strategy	NO_x [g/kWh]	HC [g/kWh]	CO [g/kWh]	Soot [g/kWh]	bsfc [g/kWh]	CN [dBA]
pM	0.46	3.7	13.3	0.03	304	76.8
ppM	min	≤3	≤12	≤0.15	≤305	≤76

(a) IAS injector

Table 7. Reference value of the *pM* calibration and targets for the optimization of the *ppM* injection strategy at 1500×2.

Strategy	NO_x [g/kWh]	HC [g/kWh]	CO [g/kWh]	Soot [g/kWh]	bsfc [g/kWh]	CN [dBA]
pM	0.99	0.3	1.9	0.3	248	88.7
ppM	min	≤0.5	≤5	≤1.2	≤255	≤89

(a) IAP injector

Strategy	NO_x [g/kWh]	HC [g/kWh]	CO [g/kWh]	Soot [g/kWh]	bsfc [g/kWh]	CN [dBA]
pM	0.89	0.32	1.99	0.16	244	88.9
ppM	min	≤0.3	≤5	≤0.3	≤242	≤89

(b) IAS injector

Table 8. Reference value of the *pM* calibration and targets for the optimization of the *ppM* injection strategy at 2000×5.

Strategy	NO_x [g/kWh]	HC [g/kWh]	CO [g/kWh]	Soot [g/kWh]	bsfc [g/kWh]	CN [dBA]
pM	2.28	0.2	0.7	0.1	238	90.0
pMa	min	≤0.2	≤1.2	≤0.8	≤238	≤89

(a) IAP injector

Strategy	NO_x [g/kWh]	HC [g/kWh]	CO [g/kWh]	Soot [g/kWh]	bsfc [g/kWh]	CN [dBA]
pM	2.2	0.2	0.89	0.08	232.5	90.0
pMa	min	≤0.2	≤1	≤0.6	≤232	≤89

(b) IAS injector

Table 9. Reference value of the *pM* calibration and targets for the optimization of the *ppM* injection strategy at 2500×8.

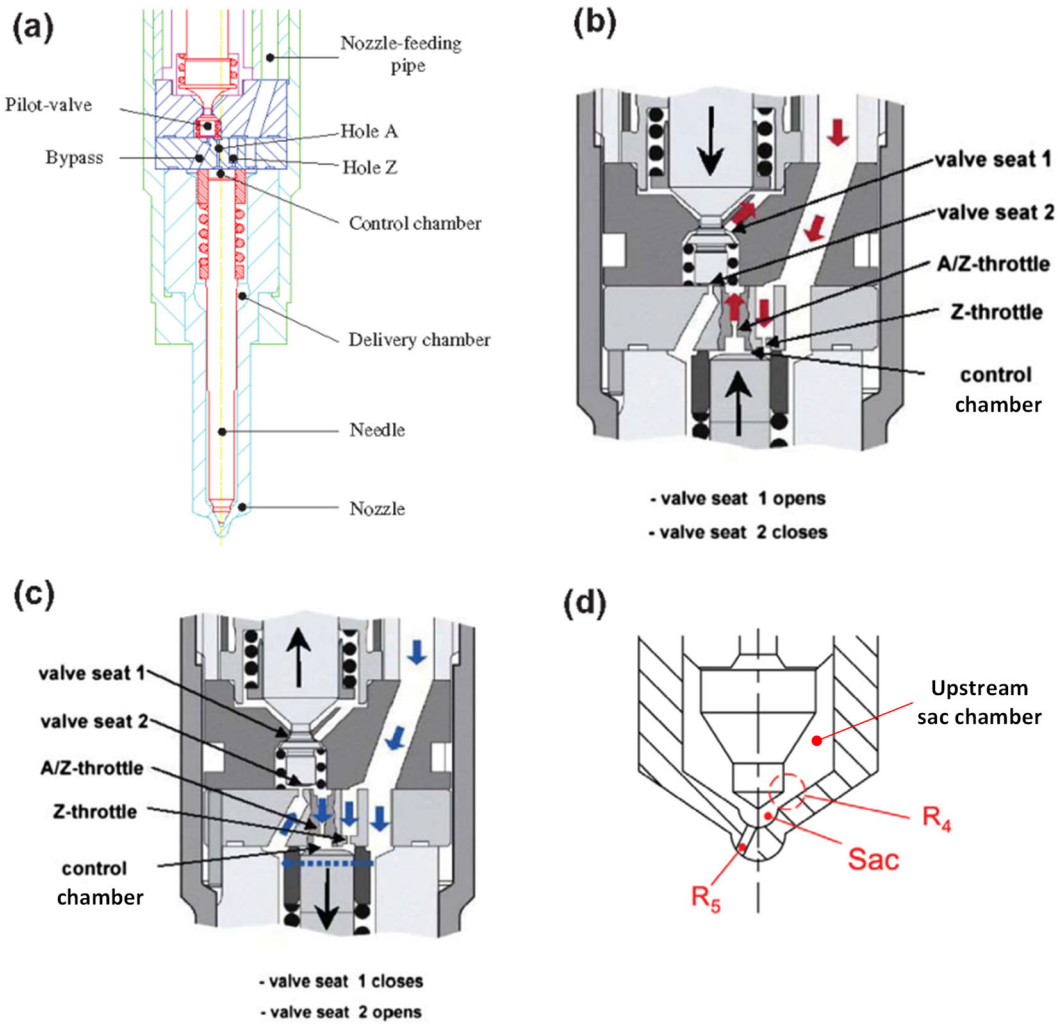

Figure 1. Indirect acting piezoelectric injector: (a) Main and pilot-valve stages. (b) Pilot-valve at opening of the needle. (c) Pilot-valve at needle closure. (d) Nozzle enlargement.

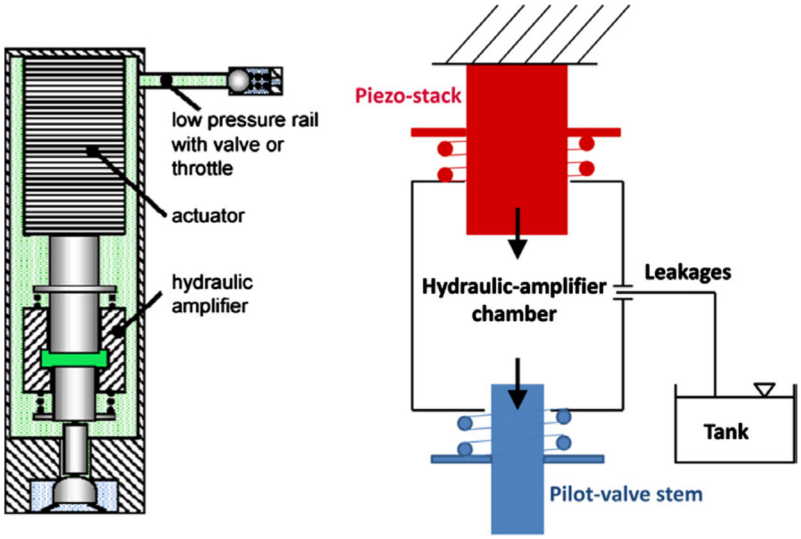

Figure 2. Hydraulic amplifier of the IAP injector.

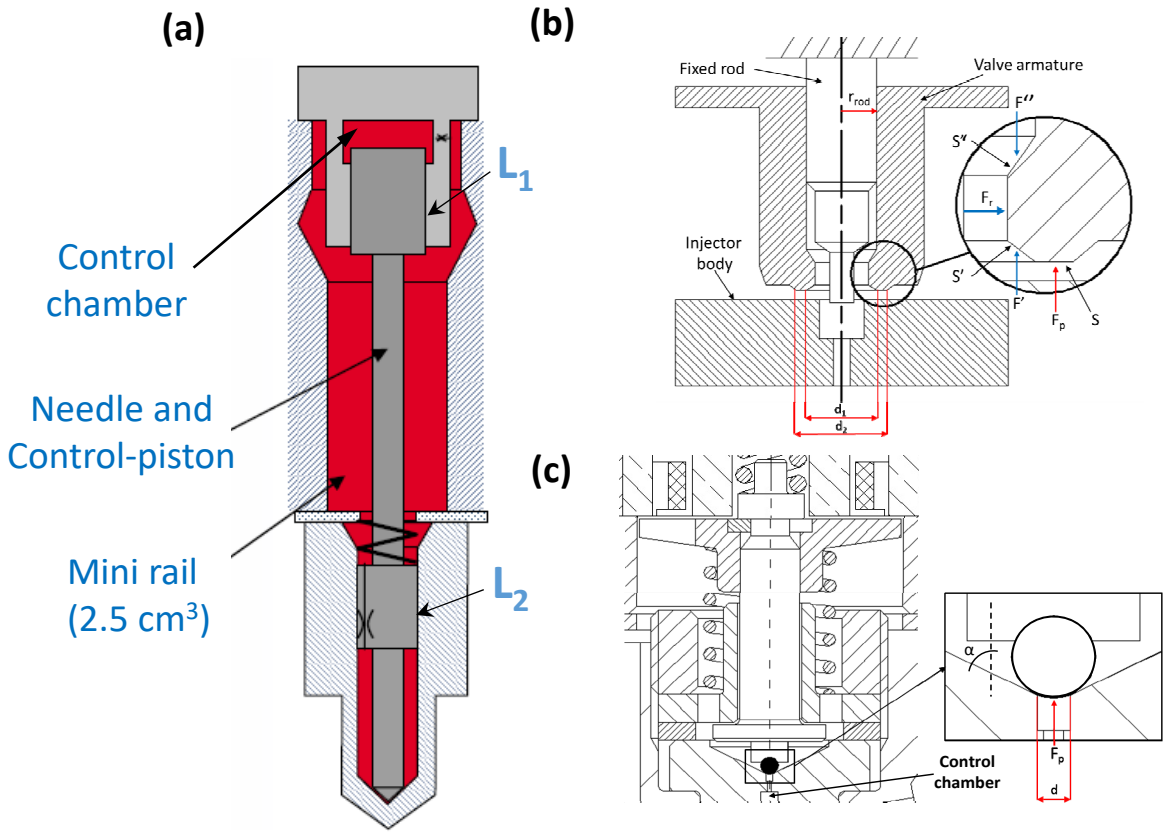

Figure 3. Solenoid injector. (a) Injector hydraulic circuit scheme. (b) Pressure balanced pilot-valve. (c) Standard pilot-valve.

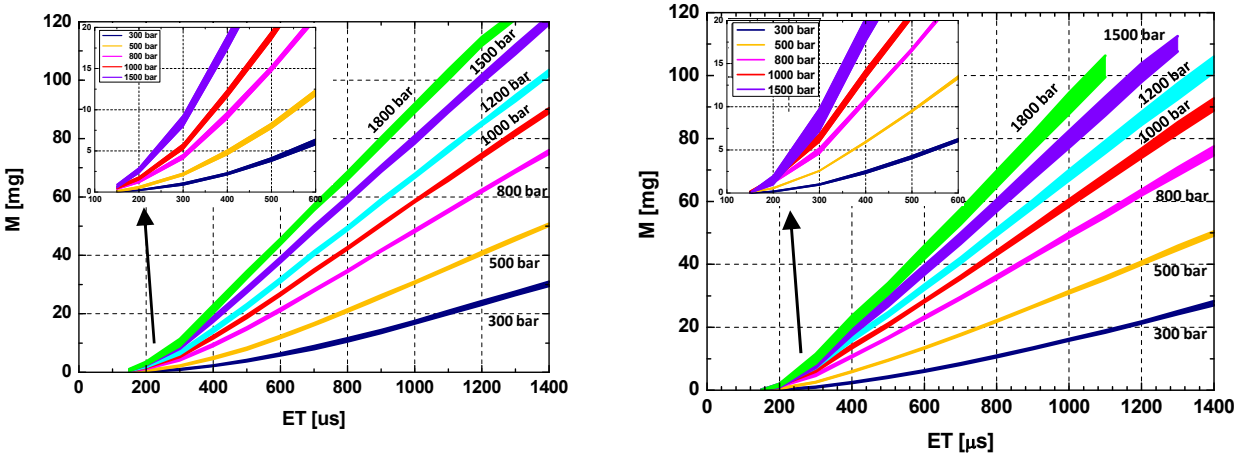

(a) IAP (b) IAS

Figure 4. Injector characteristics.

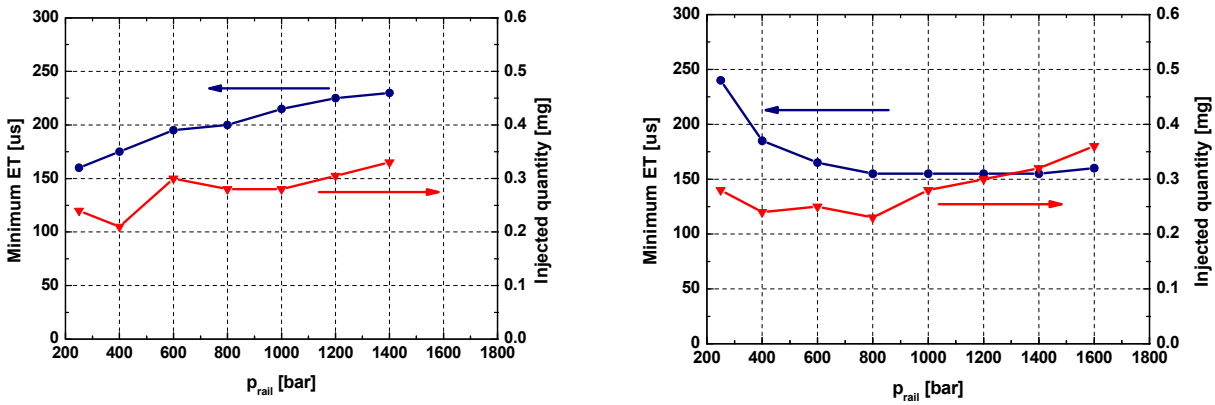

(a) IAP (b) IAS

Figure 5. Minimum energizing time and minimum injected quantity.

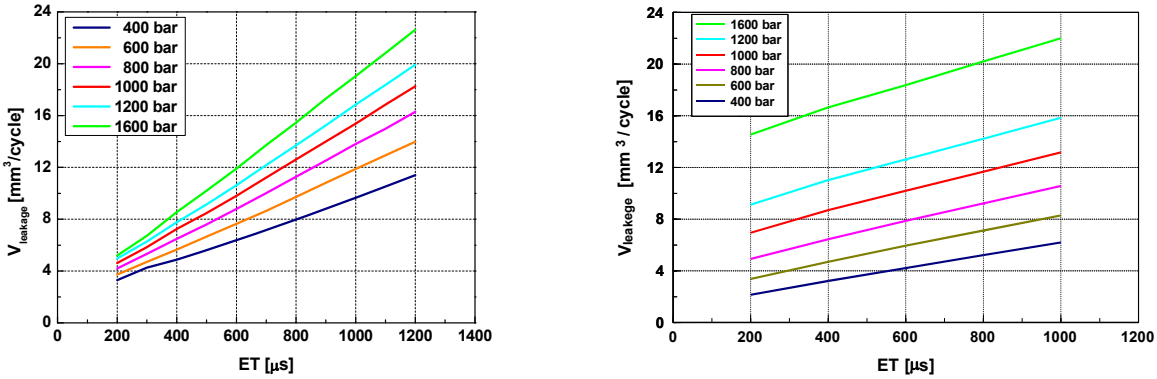

(a) IAP (b) IAS

Figure 6. Injector leakage (volume measured at 30°C per engine cycle).

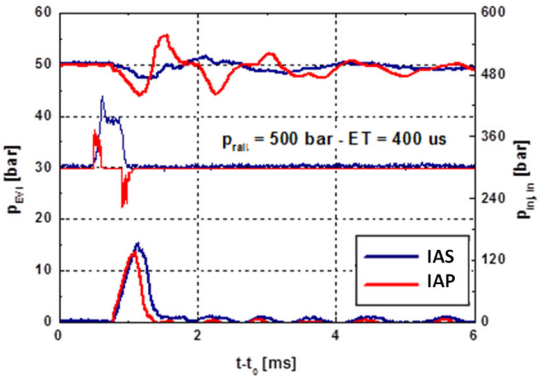

Figure 7. Injection rate (p_{EVI}) and $p_{inj,in}$ time histories (small Injected quantity).

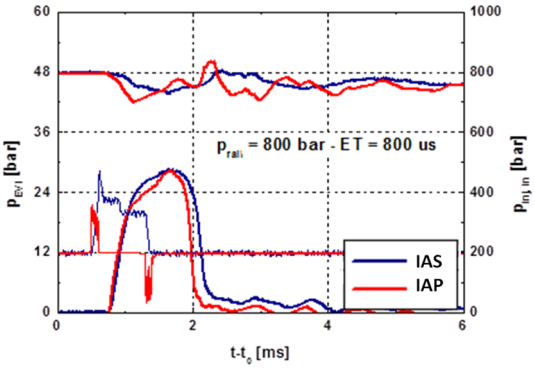

Figure 8. Injection rate (p_{EVI}) and $p_{inj,in}$ time histories (medium Injected quantity).

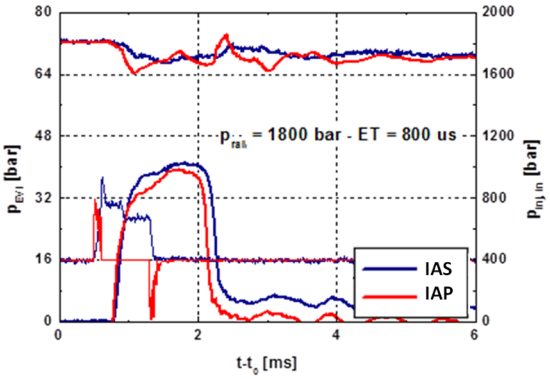

Figure 9. Injection rate (p_{EVI}) and $p_{inj,in}$ time histories (large injected quantity).

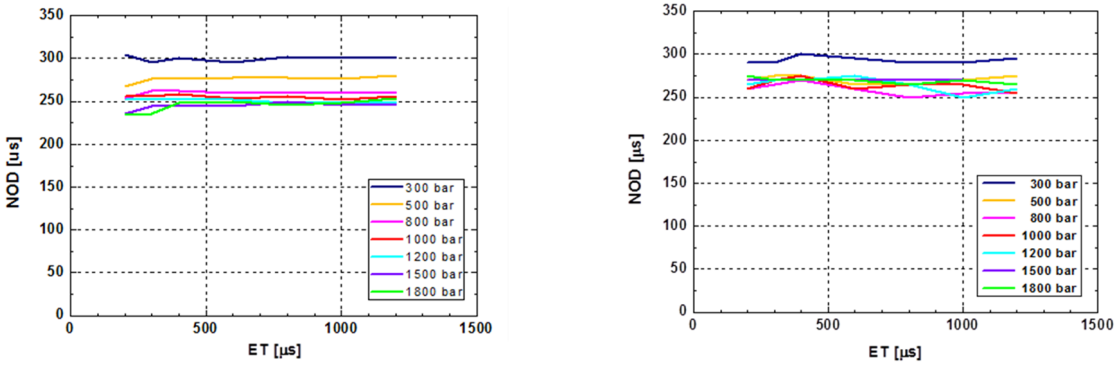

(a) IAP (b) IAS

Figure 10. Nozzle opening delay.

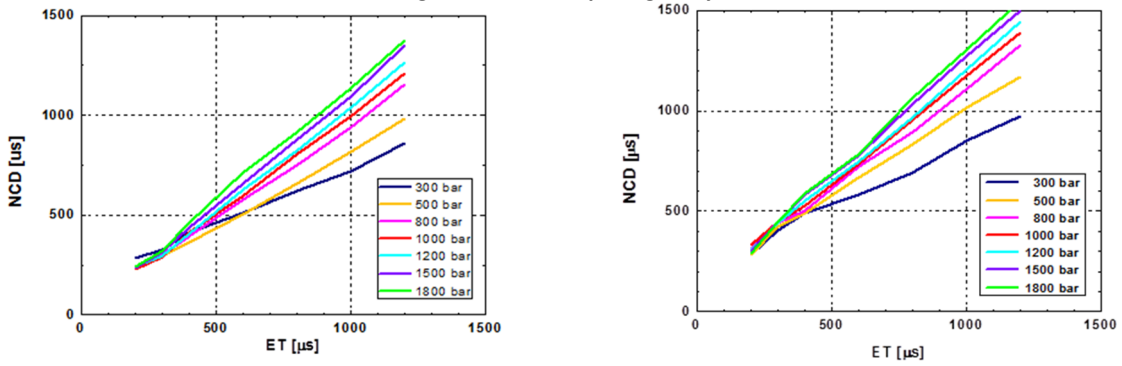

(a) IAP (b) IAS

Figure 11. Nozzle closure delay.

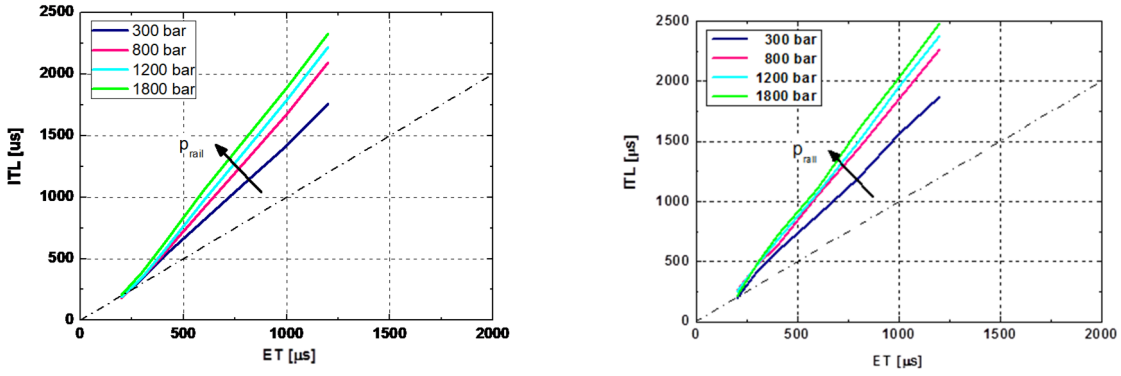

(a) IAP (b) IAS

Figure 12. Injection temporal length.

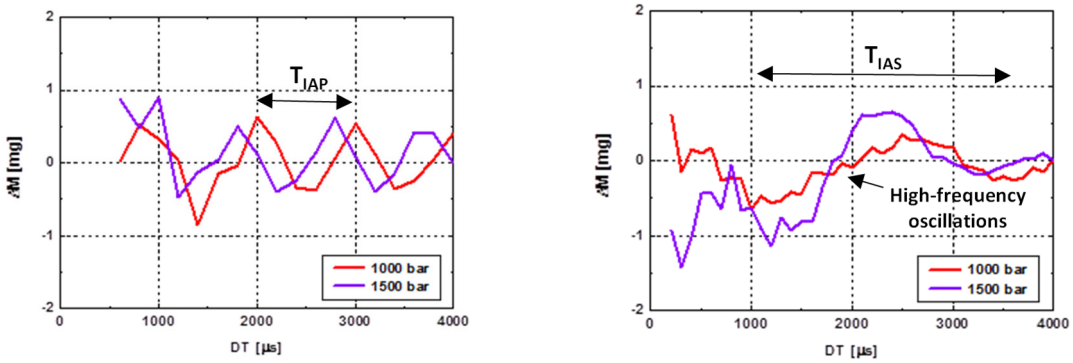

(a) IAP (b) IAS

Figure 13. Injected mass fluctuations versus dwell time at different p_{nom} values for the pilot-main injections.

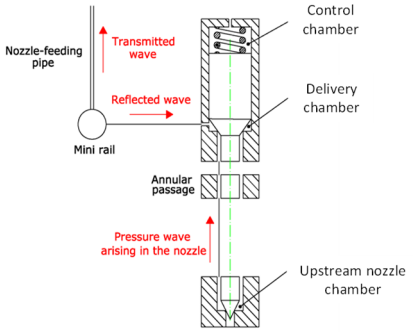

Figure 14. Fluid dynamic effect of the Minirail integrated in the IAS injector.

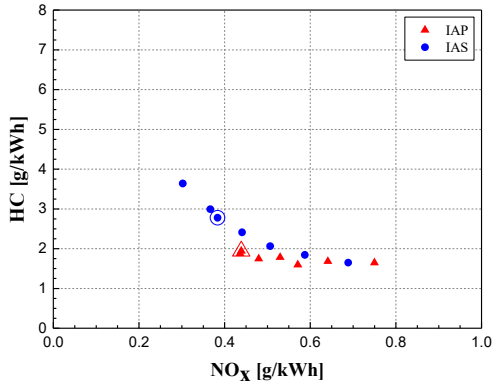

Figure 15. *HC* vs. *NO$_x$* engine out emissions along an *EGR* sweep for the *ppM* strategy (*bmep*=2 bar, *n*=1500 rpm).

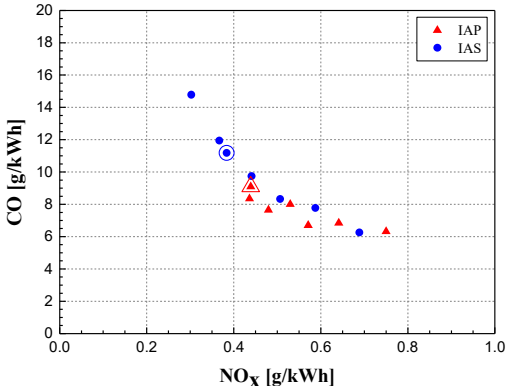

Figure 16. *CO* vs. *NO$_x$* engine out emissions along an *EGR* sweep for the *ppM* strategy (*bmep*=2 bar, *n*=1500 rpm).

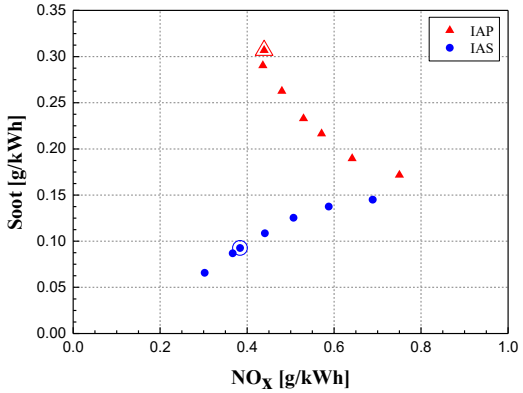

Figure 17. Soot vs. *NO$_x$* engine out emissions along an *EGR* sweep for the *ppM* strategy (*bmep*=2 bar, *n*=1500 rpm).

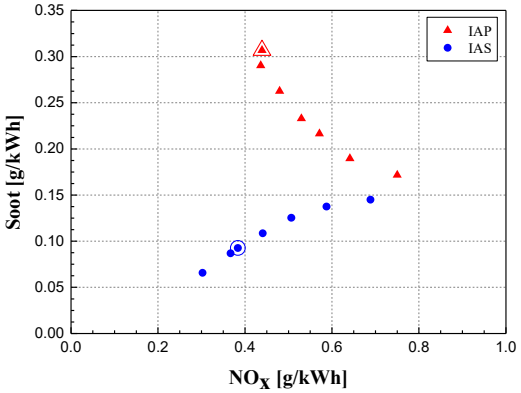

Figure 18. *CN* vs. *NO$_x$* engine out emissions along an *EGR* sweep for the *ppM* strategy (*bmep*=2 bar, *n*=1500 rpm).

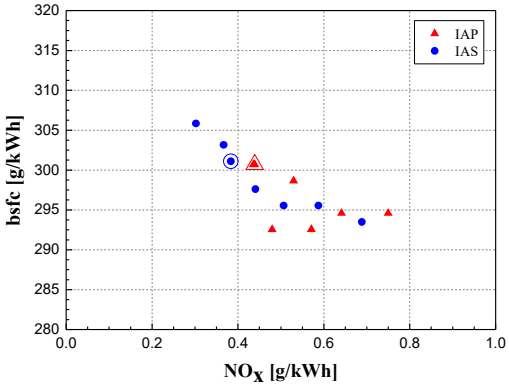

Figure 19. *bsfc* vs. *NO$_x$* engine out emissions along an *EGR* sweep for the *ppM* strategy (*bmep*=2 bar, *n*=1500 rpm).

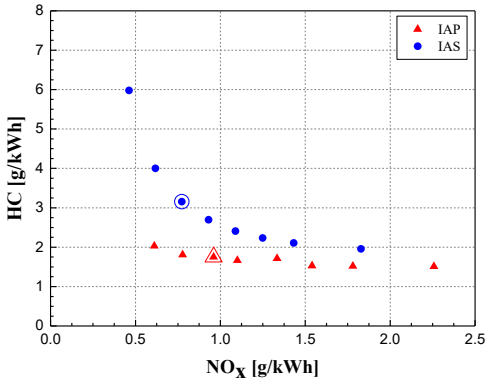

Figure 20. *HC* vs. *NO$_x$* engine out emissions along an *EGR* sweep for the *pM* strategy (*bmep*=2 bar, *n*=2000 rpm).

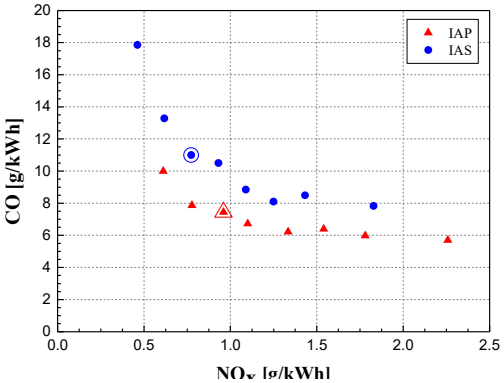

Figure 21. *CO* vs. *NO$_x$* engine out emissions along an *EGR* sweep for the *pM* strategy (*bmep*=2 bar, *n*=2000 rpm).

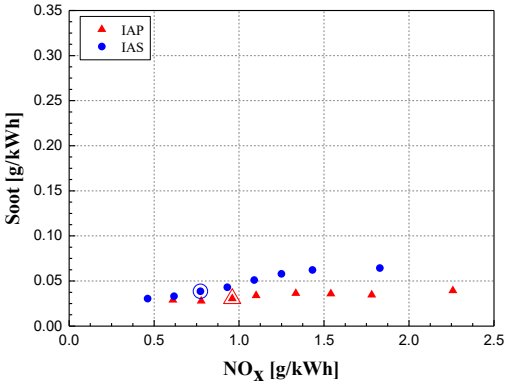

Figure 22. Soot vs. *NO$_x$* engine out emissions along an *EGR* sweep for the *pM* strategy (*bmep*=2 bar, *n*=2000 rpm).

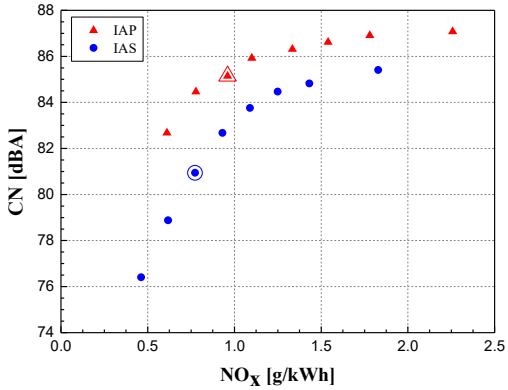

Figure 23. *CN* vs. *NO$_x$* engine out emissions along an *EGR* sweep for the pM strategy (*bmep*=2 bar, *n*=2000 rpm).

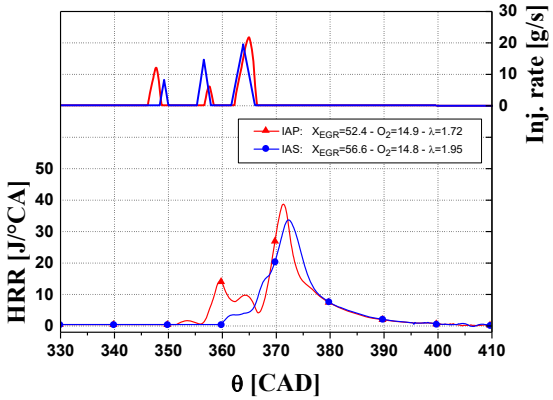

Figure 24. *HRR* versus θ distributions for the baseline points of the *ppM* strategy (*bmep*=2 bar, *n*=1500 rpm).

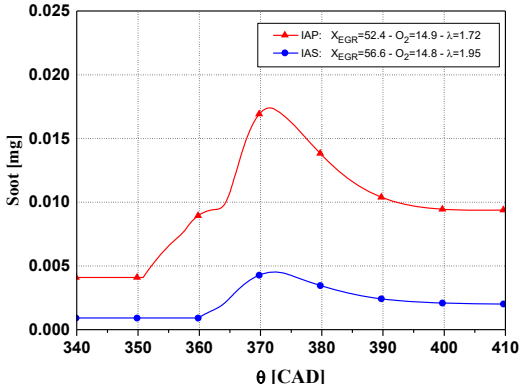

Figure 25. Soot versus θ distributions for the baseline points of the *ppM* strategy (*bmep*=2 bar, *n*=1500 rpm).

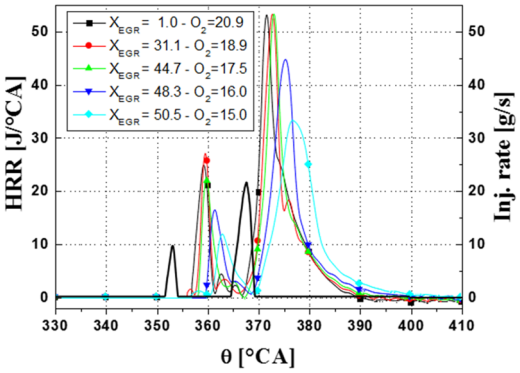

Figure 26. *HRR* versus θ distributions along an *EGR* sweep for the IAP injector (*pM* strategy, *bmep*=2 bar, *n*=1500 rpm)

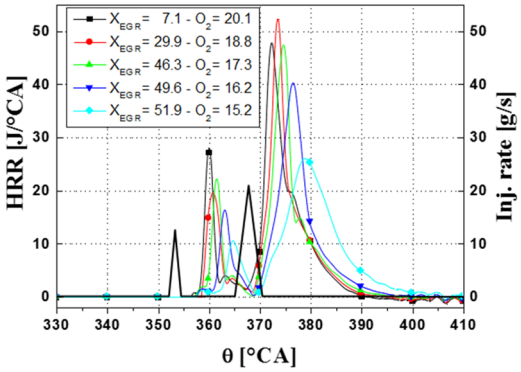

Figure 27. *HRR* versus θ distributions along an *EGR* sweep for the IAS injector (*pM* strategy, *bmep*=2 bar, *n*=1500 rpm)

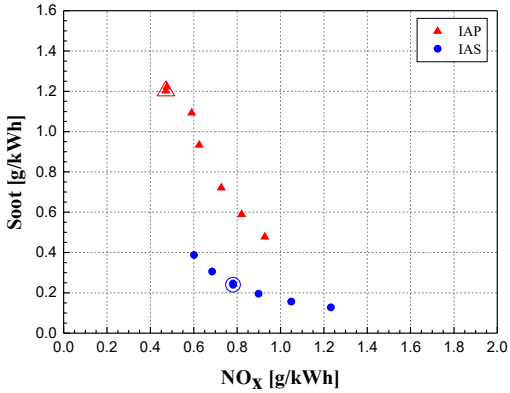

Figure 28. Soot vs. *NO$_x$* engine out emissions along an *EGR* sweep for the *ppM* strategy (*bmep*=5 bar, *n*=2000 rpm).

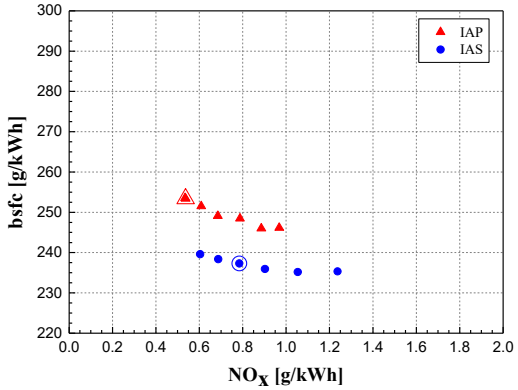

Figure 29. *bsfc* vs. *NO$_x$* engine out emissions along an *EGR* sweep for the *ppM* strategy (*bmep*=5 bar, *n*=2000 rpm).

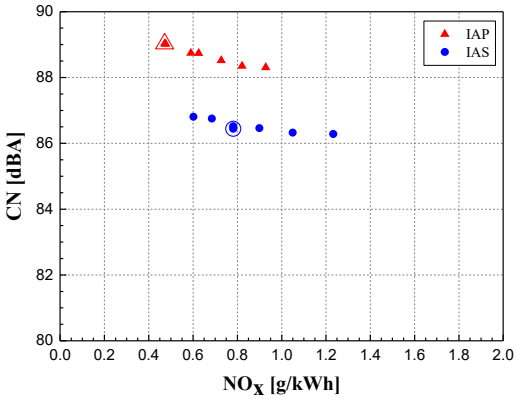

Figure 30. *CN* vs. *NO$_x$* engine out emissions along an *EGR* sweep for the *ppM* strategy (*bmep*=5 bar, *n*=2000 rpm).

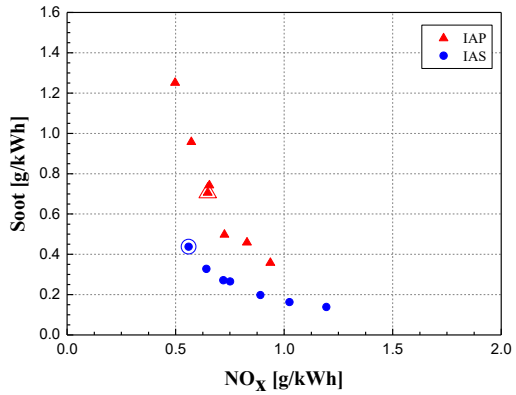

Figure 31. Soot vs. *NO$_x$* engine out emissions along an *EGR* sweep for the *pMa* strategy (*bmep*=5 bar, *n*=2000 rpm).

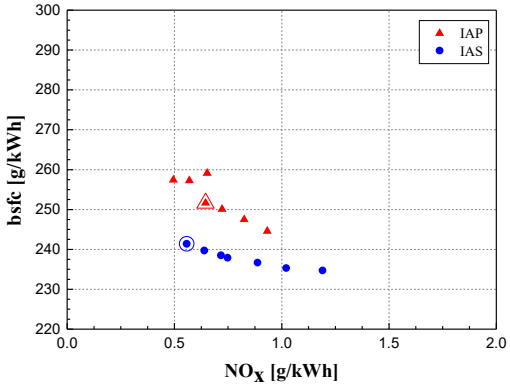

Figure 32. *bsfc* vs. *NO$_x$* engine out emissions along an *EGR* sweep for the *pMa* strategy (*bmep*=5 bar, *n*=2000 rpm).

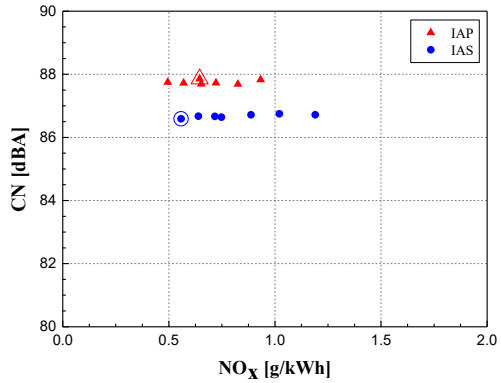

Figure 33. *CN* vs. *NO$_x$* engine out emissions along an *EGR* sweep for the *pMa* strategy (*bmep*=5 bar, *n*=2000 rpm).

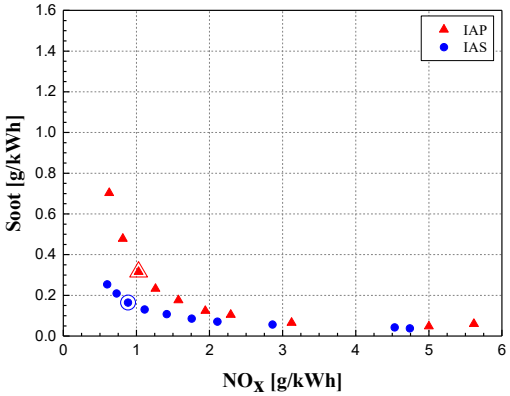

Figure 34. Soot vs. *NO$_x$* engine out emissions along an *EGR* sweep for the *pM* strategy (*bmep*=5 bar, *n*=2000 rpm).

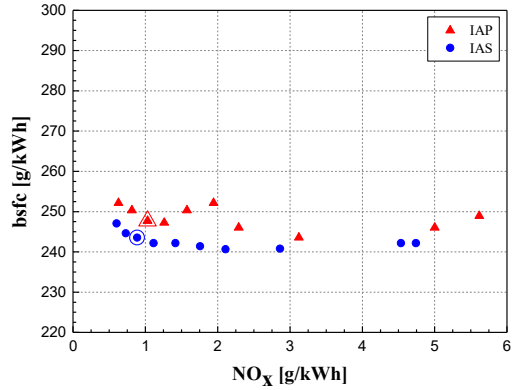

Figure 35. *bsfc* vs. *NO$_x$* engine out emissions along an *EGR* sweep for the *pM* strategy (*bmep*=5 bar, *n*=2000 rpm).

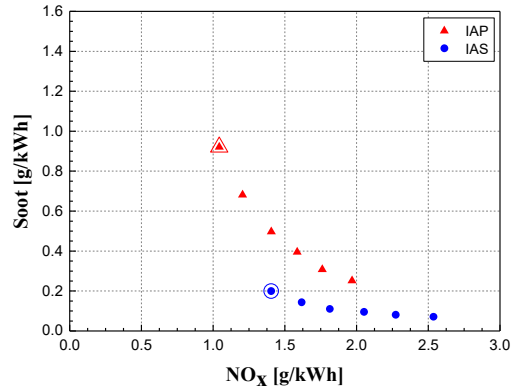

Figure 36. Soot vs. *NO$_x$* engine out emissions along an *EGR* sweep for the *pMa* strategy (*bmep*=8 bar, *n*=2500 rpm).

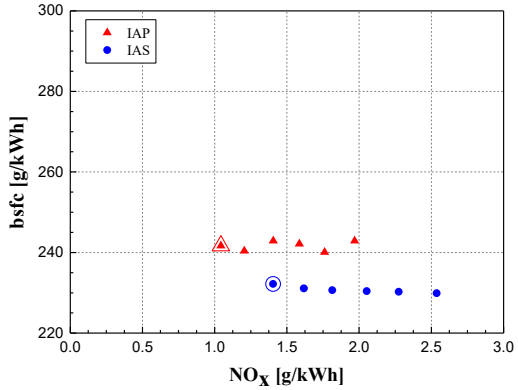

Figure 37. *bsfc* vs. *NO$_x$* engine out emissions along an *EGR* sweep for the *pMa* strategy (*bmep*=8 bar, *n*=2500 rpm).

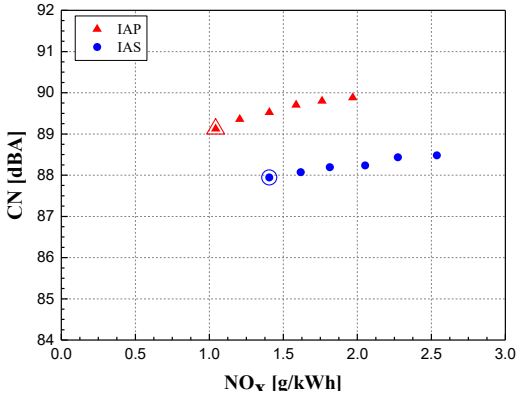

Figure 38. *CN* vs. *NO$_x$* engine out emissions along an *EGR* sweep for the *pMa* strategy (*bmep*=8 bar, *n*=2500 rpm).

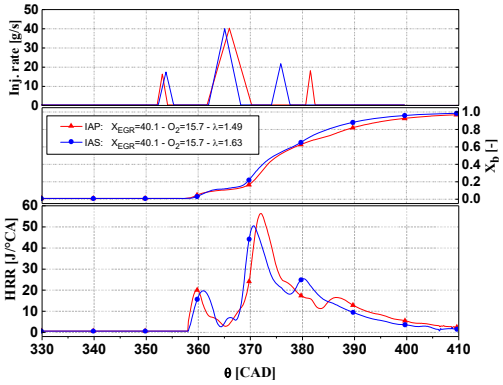

Figure 39. *HRR,* injection rate and x_b versus θ distributions (*pMa* strategy, *bmep*=5 bar, *n*=2000 rpm).

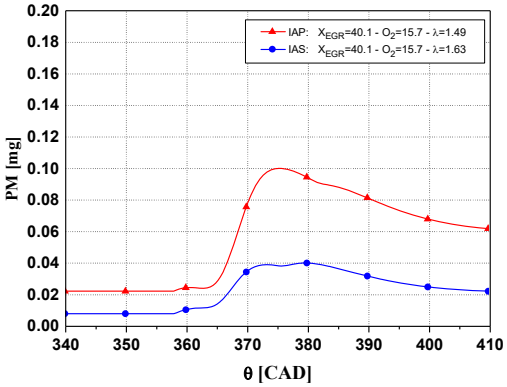

Figure 40. Soot versus θ distributions for the baseline points of the *pMa* strategy (*bmep*=5 bar, *n*=2000 rpm).